for the system. These initial mole fractions for each gas may be found in Table 3.4 below. (The system is pre-seeded with a small quantity of charged species to avoid computational errors.)

Table 3.4: Initial conditions of starting species for air and steam plasma simulations.

		Air Case	Steam Case
Gas Phase Species	N2	0.766	0
	N2+	1×10^{-20}	1×10^{-20}
	O2	0.203	0
	E	1×10^{-20}	1×10^{-20}
	H2O	3.521×10^{-2}	1.000
Liquid Phase Species	H2O_L	1.000	1.000
	H2O+_L	1×10^{-14}	1×10^{-14}
	O2_L	6.930×10^{-6}	6.930×10^{-6}
	N2_L	3.030×10^{-6}	3.030×10^{-6}
	E_L	1×10^{-14}	1×10^{-14}

The plasma was modeled through applying a power deposition profile as a function of time to the system. In the experiments in this thesis, the power deposition profiles were taken from each

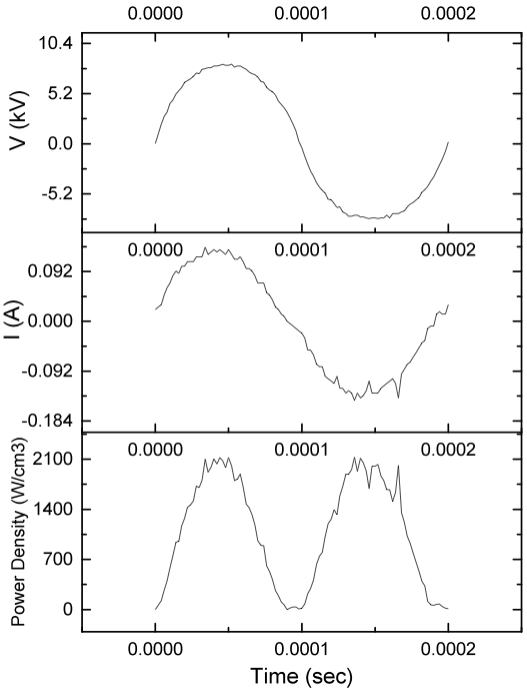

Figure 3.25: Portion of a voltage (top) and current (middle) trace of a steam discharge experiment. The calculated instantaneous power density of the plasma on the gas bubble volume is shown on the bottom.

experiment they were meant to verify. This was accomplished through using the voltage and current waveform from the oscilloscope and calculating the instantaneous power deposition of the plasma discharge onto the volume of the gas bubble sphere at each time step (see Figure 3.25). This power density profile for one voltage cycle is repeated throughout the integration time set (0.1 seconds).

The simulation is run, and from the change in species density over time, production rates of various species are computed, including hydrogen peroxide, nitrate and nitrite. These rates are compared to experimentally measured results.

3.4.5 Power Measurements & Energy Efficiency

3.4.5.1 Lissajous Method

Power consumption of the discharge was ascertained using the Lissajous method, a common and accurate method used for DBD plasmas [**190**]. The Lissajous method is typically used to determine power deposition in DBD discharges. The Lissajous method was chosen over direct integration of current and voltage waveforms as it avoids error and uncertainty associated with integration of complex waveforms, such as missing fine scale structure associated with limited oscilloscope bandwidth.

In this method, first discussed by Manley [**326**], the charge, Q, accumulated in the system is plotted versus the applied voltage, V_1, and the area of this figure over a cycle corresponds to the deposited power [**190**]. The voltage across a sense capacitor of capacitance C is used to determine charge transferred as a function of time (3.12).

$$Q(t) = V_c(t) * C \tag{3.12}$$

The power deposited by the plasma per discharge cycle, P, may be determined via

$$P = f \int_{t_0 - T/2}^{t_0 + T/2} V_1(t) * V_c(t) * C dt = f \int_{t_0 - T/2}^{t_0 + T/2} V_1(t) * Q(t) dt \tag{3.13}$$

In the previous equation, f is the frequency of the discharge, t_0 is an arbitrary reference time used in the calculation, and T is the period of the discharge (and therefore $t_0 \pm T/2$ is the time related to half a discharge cycle) [**327**].

A typical Lissajous figure is shown in Figure 3.26. Using the formulae above, the power of the given figure was calculated to be approximately 260 W. Other breakdown information that can be obtained through the use of a Lissajous figure may be viewed in Figure 3.27 (n.b., notation changes to U for applied voltage).

Through analysis of the Lissajous shape, insight into the nature of the discharge can be gleaned. For example, the dielectric capacitance and total gap capacitance can be obtained as well as the actual breakdown voltage. Additional discharge parameters that may be obtained from a Lissajous figure include the charge ($Q_{pk\text{-}pk}$), charge discharged (Q_d), charge transferred per half cycle ($Q_{trans.}$), minimum burning voltage necessary to operate the discharge (U_{min}), capacitance of the dielectric (C_d), and total capacitance (C_t), illustrated on the idealized Lissajous figure, which appears as a parallelogram shown in Figure 3.27. [**327**]. The Lissajous method was the primary method used in this work to calculate deposited power.

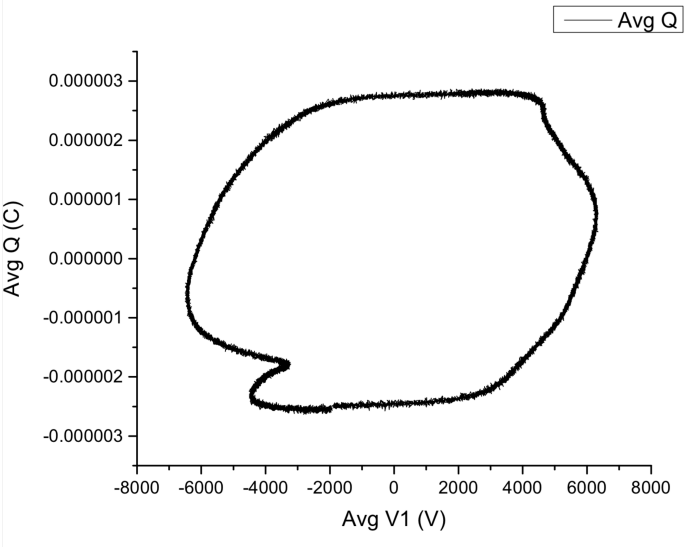

Figure 3.26: Typical Lissajous figure of the steam discharge in operation. This figure corresponds to a discharge of 260 W.

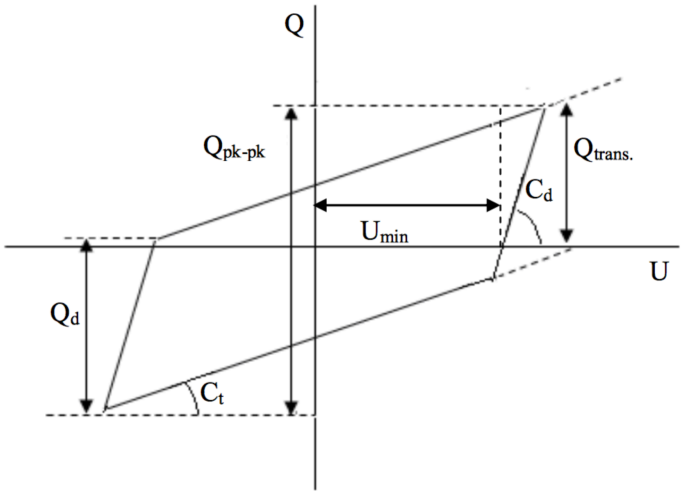

Figure 3.27: Discharge parameters from a Lissajous figure. From [327**].**

The relationship between the various system capacitances that may be determined from a Lissajous figure is given by [**327**]

$$\frac{1}{C_T} = \frac{1}{C_g} + \frac{1}{C_d} \tag{3.14}$$

where C_g is the capacitance of the gas.

3.4.5.2 Energy Efficiency

The field of plasma-driven water treatment is diverse, with a multitude of different discharge types and applicators, each with unique operating conditions and parameters. Additionally, research groups examine different wastewater simulants, which have their unique chemistries. Various methods of normalizing the resulting data so as to compare the various methods include assessing species production efficiency (e.g., hydrogen peroxide production evaluation by Locke and Shih [**177**]) and decomposition efficiency (e.g., energy efficiency by Malik [**50**]). The G_{50} value (3.15), proposed by Malik [**50**], is a measure of the energy required to decompose 50% of the pollutant:

$$G_{50} = \frac{1.8\times10^6 C_0 V_0 M}{P t_{50}} \tag{3.15}$$

where G_{50} is given in grams per kilowatt-hour (g kWh^{-1}); C_0 is the molar concentration of the pollutant at $t = 0$ (M, or mol/L); V_0, the treated volume (L); M, pollutant molecular weight (g/mol); P, power (W); and t_{50}, the processing time necessary to remove 50% of the pollutant (s). The determination of t_{50} requires the use of some mass spectrometry; in this dissertation, it is determined either through the use of a spectrophotometer or HPLC measurements. A larger G_{50} value indicates a more energy efficient process. The sources discussed in this dissertation have G_{50} values that range from roughly 0.1 g kWh^{-1} (the steam discharge in its most inefficient state) to over 10 g kWh^{-1} (the air-feed microdischarge). In comparison to the data presented in the review by Malik [**50**], G_{50} values of 5 and greater fall into the top third of energy efficient plasma reactors.

Chapter 4:

Single Bubble Breakdown: Breakdown Mechanisms and Behaviors of Attached and Unattached Bubbles

4.1 Overview

As previously discussed, non-thermal plasma discharges have demonstrated the ability to decompose dissolved organic contaminants via advanced oxidation-induced mineralization, making them a strong candidate for the next generation of water purification technologies. However, a myriad of unknowns obscure the path towards a comprehensive device. Practical implementation of plasma-based water purification methods relies firstly on understanding of the physics of breakdown in water and secondly on the resulting plasma-driven chemistry and decomposition mechanisms, discussed in later chapters. Electrical and decomposition efficiency are two additional considerations as well. This chapter describes the experimental investigation aimed at understanding the breakdown physics of the plasma-liquid-gas system. The experiments detailed in this chapter fall into two categories: (1), break down in isolated bubbles including understanding breakdown voltage scaling with bubble size and internal pressure and (2), macroscopic effects of high electric fields on the water-gas interface and the implications of such effects.

The physics of gas bubbles in liquids subjected to high fields, streamers and general electrical discharges is complex and highly effected by a multitude of factors [**160**,**274**,**328**]. Much can be learn by simplifying the system to include only a single bubble or an ensemble of only a few (<5 bubbles). It is this approach, following that of Sommers [**72**,**107**] that is taken herein. The bubbles studied are either attached to an electrode or trapped in an acoustic field, such that they are held motionless, thereby eliminating the effects of electrode processes.

For all experiments, room air was used as the feed gas to form the bubbles. Voltage is applied to acoustically trapped bubbles using a point to plane electrode geometry (Figure 3.3), and electrode attached bubbles are investigated in a plane to plane electrode geometry. Figure 3.4).

4.2 Plasma Production in Unattached Bubbles

Experimental observations and electromagnetic simulations of plasma discharges in acoustically levitated bubbles are described, with the focus of determining and analyzing physical scalings and parameters related to the discharge mechanics.

4.2.1 Effect of Bubble Size

The size of the bubble was observed to have an effect on the discharge character. Figure 4.1 and Figure 4.2 depict two bubbles, one large (1.2 mm diameter) and a smaller bubble (0.4 mm diameter), both at roughly the same distance from the electrode (0.18 mm and 0.19 mm, respectively). Plasma was ignited in the large bubble upon application of 11.8 kV pulse, and in the small bubble with a pulse of 12.5 kV. In general, breakdown structures in large bubbles exhibit localized, glow-like discharges. In Figure 4.1, the structure appears to have tendril-like streamers that emanate from the glow-like point closest to the powered electrode and hug the water-air boundary layer. Smaller bubbles also exhibit surface-hugging streamers, but electrohydraulic distortion of smaller bubbles is commonly observed (see Figure 4.2). This distortion only occurs during application of the high voltage pulse, and the bubble may return to its original size and shape after the field ceases. If the distortion is large enough, the bubble may be destroyed (e.g., see [**72**]). The relatively larger perturbations on the smaller bubble may be related to excitation of resonant capillary waves consistent with bubble size [**106**].

4.2.2 Effect of Bubble and Electrode Separation Length

When producing plasma in isolated bubbles, a liquid-phase streamer is sometimes observed to bridge the bubble-electrode gap. The presence of this connecting streamer was observed to depend on the gap length between the bubble and the electrode. A large number of observations in these experiments saw that connecting water streamers did not appear for bubbles with small (≤ 0.2 mm) gap lengths, while large gap lengths tend to produce connecting streamers.

In the case of small gap lengths (i.e., bubbles close to the electrode), two discharges are observed: a localized discharge about the electrode tip and a discharge within the bubble. This electrode discharge may be seen in Figure 4.1 through Figure 4.3 (distances between electrode tip and bubble were 0.18 mm, 0.19 mm, and 0.05 mm, respectively). In these circumstances, there exists a glow-like discharge about the electrode tip and a somewhat distinct discharge within the bubble.

This phenomenon is believed to be a direct visual example of the Meek criterion and streamer initiation. If the separation distance between bubble and electrode is smaller than the critical distance necessary for streamer formation, that critical distance is met within the bubble or at the gas-liquid boundary. As the streamer head is now within the bubble gas, the associated self-sustaining electric field of the streamer is primarily interacting within the gas phase as opposed to the liquid phase. This results in the majority of ionization and photon production occurring within the bubble, giving rise to a "separated" discharge look (i.e., as opposed to the bridged discharge seen in Figure 4.4.) This results in the phenomenon seen in Figure 4.1, Figure 4.2, and Figure 4.3. The Meek criterion is calculated through electric field simulation (through *Maxwell*, example given in Figure 4.6).

The results in Figure 4.5 (also given in Table 4.1) give the critical distance for streamer initiation for various ionization products (M = 20 through 30) based on the results of the simulated electric field at the bubble surface. A range of ionization products is given to account for the estimation of the Meek criterion From these calculated values of the electric field at the bubble surface, it is seen that the measured separation length between electrode and bubble correlates with the calculated critical distance for streamer initiation.

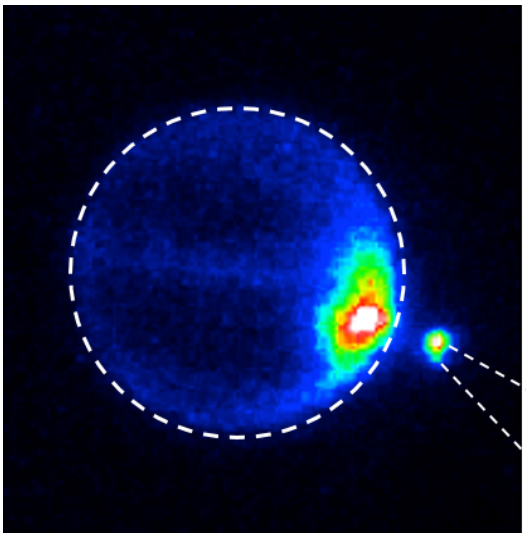

Figure 4.1 (left): Large bubble, 1.68 mm diameter, 11.8 kV applied, 0.18 mm gap. The small bright point to the right of the bubble is the electrode tip. [329**]**

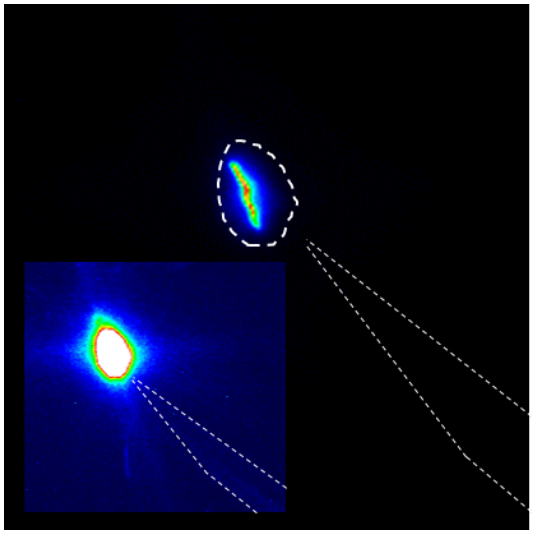

Figure 4.2 (right): Small bubble, 0.40 mm diameter, 12.5 kV applied, 0.19 mm gap. The main figure depicts the main streamer, while the insert depicts the deformation of the bubble during discharge (same image, different intensities) [329**].**

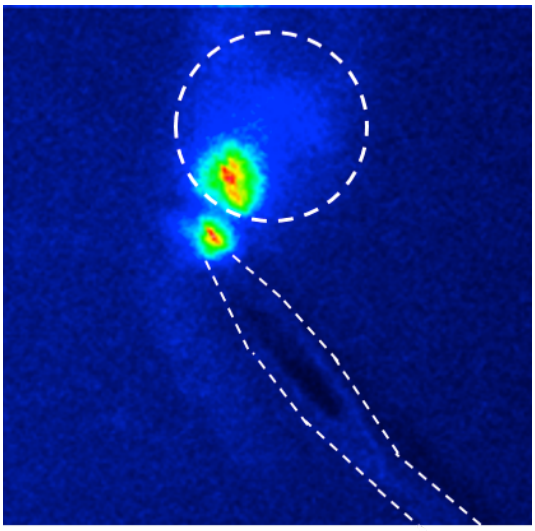

Figure 4.3 (left): 0.77 mm diameter, 10.4 kV applied, 0.05 mm gap, plasma in bubble and on electrode tip. [329**]**

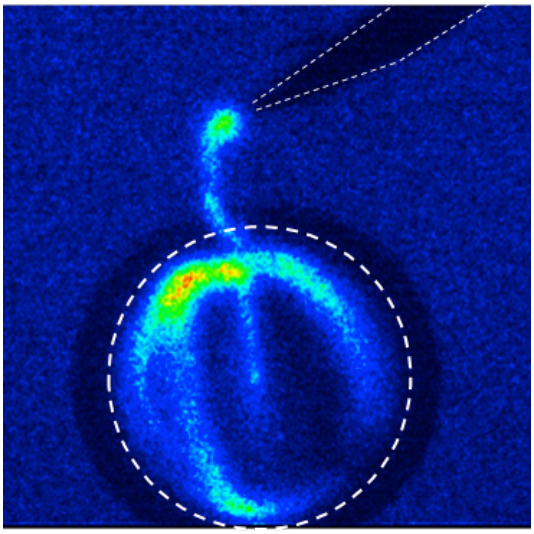

Figure 4.4 (right): 1.25 mm diameter, 12 kV applied, 0.37 mm gap, plasma in bubble and between bubble and electrode. [329**]**

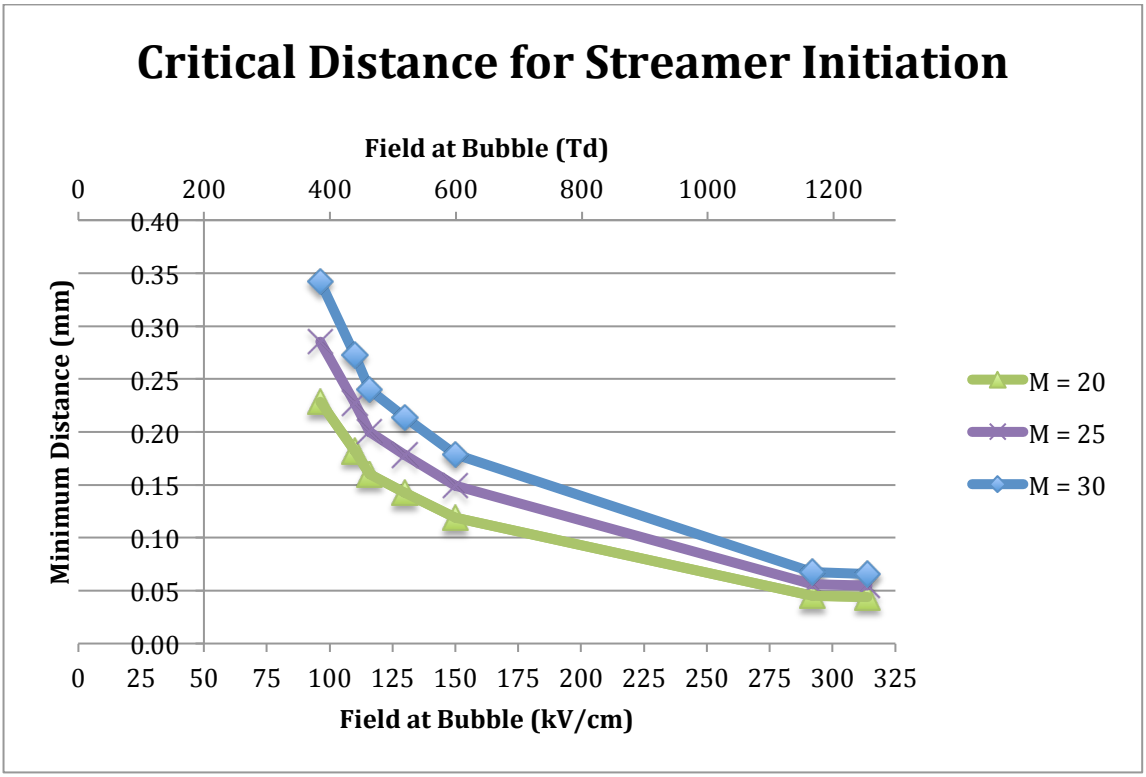

Figure 4.5: Critical distance for streamer initiation for various ionization products.

Table 4.1: Experiment versus simulation (tabulated results from Figure 4.5). Critical distances for streamer initiation for various ionization products.

EXPERIMENT			SIMULATION				
Bubble	Field at Bubble (kV/cm)	Separation Distance (mm)	Field at Bubble (kV/cm)	Field at Bubble (E/N)	Critical Distance for Streamer Formation (mm)		
					M = 20	*M = 25*	*M = 30*
Figure 4.1	~110	0.18	96.3	384.6	0.23	0.29	0.34
			110	439.3	0.18	0.23	0.27
			116	463.2	0.16	0.20	0.24
Figure 4.2	~130	0.19	130	519.1	0.14	0.18	0.21
			150	599.0	0.12	0.15	0.18
Figure 4.3	~300	0.05	292	1.166×10^3	0.04	0.06	0.07
			314	1.254×10^3	0.04	0.05	0.07

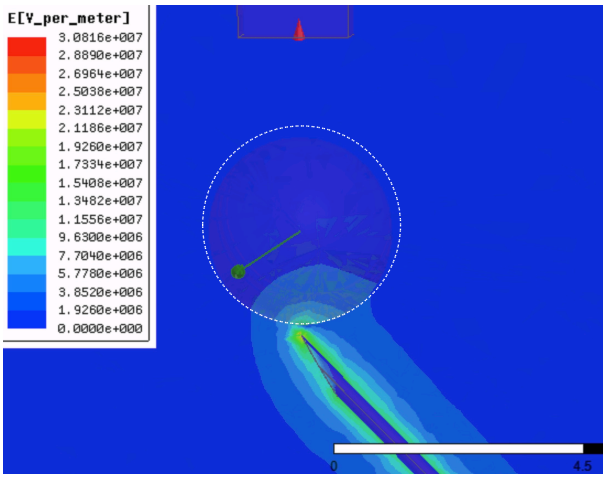

Figure 4.6: *Maxwell* electric field simulation of bubble. White scale bar is equal to 4.5 mm.

At larger separation distances, the propagation of liquid streamers from the electrode to the surface of the bubble has also been observed, resulting in the plasma formation within the bubble (see also [**107**]). This can clearly be observed in Figure 4.4. In this case, it is a liquid streamer that ignites a gas streamer in the bubble. While discharges such as these may appear to have faint bridging, such as in Figure 4.1, these are considered as separate in comparison to discharges such as depicted in Figure 4.4, where the critical length for streamer initiation is satisfied within the water intermediate between electrode and bubble. Further study will determine if faint bridging in discharges such as in Figure 4.1 is due to x_{crit} being on the verge of the bubble boundary or an experimental equipment factor (e.g., iCCD chip sensitivity).

4.2.3 Plasma Propagation Between Multiple Bubbles

Possible experimental observations of streamer hopping are discussed. As discussed previously in Chapter 2, streamer hopping in microbubbles (1 to ~100 μm in diameter) was postulated by Qian et al. [**330**] and computationally supported by Babaeva and Kushner [**114**].

An air bubble 2 mm in diameter was placed between parallel plate electrodes approximately 2.18 mm in separation (Figure 4.7). Upon the application of high voltage (9.62 kV), the bubble disintegrates, and the electrode gap is filled with small bubbles (sizes ranging from a few hundreds of microns to tens of microns and perhaps smaller[31]). Successive voltage pulses of roughly the same amplitude (9.64 ± 0.1 kV for ~20 pulses) either do not produce breakdown of

[31] The resolution of these images is 11 μm/pixel and prevents further comment.

any kind or result in sparks that are branched in structure, zigzagging sharply between air bubbles as in Figure 4.8.

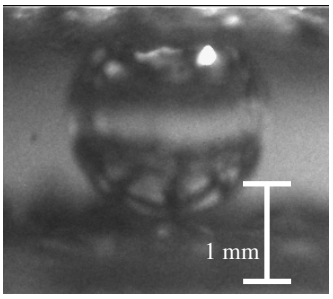

Figure 4.7: 2 mm diameter air bubble between parallel plate electrodes, pre-voltage application.

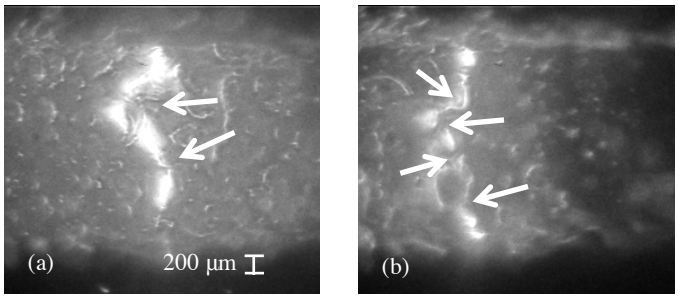

Figure 4.8: Possible evidence of streamer hopping. Applied voltages 9.58 kV (a) and 9.56 kV (b). Arrows indicate various bubble locations.

This observed streamer structure is believed due to the ignition of bubbles preceding the streamer head (indicated in Figure 4.8), producing the angular discharge path. If the bubbles are not facilitating breakdown in the sense of providing "seeds" for new streamers, an alternative explanation is the bubbles are influencing the discharge path through the liquid, producing a kink instability-like structure. This influence would be due to the change in dielectric constants between air ($\varepsilon_{dry\ air} \approx 1$) and water ($\varepsilon_w \approx 80$), and the effect of this change has on the polarization of the medium and the resulting streamer propagation [**331**,**332**]. However, as breakdown is only observed to occur in this zigzagging manner, it is believed to be evidence of streamer hopping.

4.3 Breakdown Scaling[32]

Of particular interest is the voltage required to breakdown a bubble immersed in liquid water and how it scales with bubble size, bubble gas composition and internal pressure. In this section, a complete examination of bubble breakdown voltage with the aforementioned parameters is presented [**333**,**334**].

4.3.1 Pressure in the bubble

The total pressure within a bubble immersed in water is given as

$$P_{tot} = P_{surf\ ten} + P_{fluid}\ ,$$

(4.1)

[32] Work presented in this section included in various forms in article submitted to Journal of Physics D: John E. Foster, Sarah N. Gucker, Bradley S. Sommers, Maria M. Garcia "A Review of Plasma Ignition in Liquid," submitted Feb. 2015.

where $P_{surf\ ten}$ is the pressure contribution due to surface tension, P_{fluid} is the pressure in the liquid at the bubble wall, (taken here to be 762.8 Torr, see following discussion).

In addition to pressure caused by the surrounding liquid, gas bubbles in liquids will experience an additional pressure due to the surface tension ($P_{surf\ ten}$) of the interface between the two media. This pressure differential corresponds to the surface tension of the liquid (γ) and the radii of curvature of the bubble (below; R_1, R_2[33]). This is described via the Young-Laplace equation given in (4.2 [**335**].

$$\Delta P_{surf\ ten} = \gamma * \left(\frac{1}{R_1} + \frac{1}{R_2}\right)$$

(4.2)

For a sphere, $R = R_1 = R_2$, thus the surface tension term for pressure across the bubble interface is

$$P_{surf\ ten} = \frac{2\gamma}{R}.$$

(4.3)

The additional pressure due to capillary pressure forces on the bubbles examined here (diameters ranging from 0.3 mm to 1.7 mm) was determined to be roughly 2 Torr on average, and approximately 4 Torr at most, taking into account the minute temperature change (± 5 °C). This additional pressure due to surface tension becomes dominant for bubbles on the order of microns, where the added pressures is over 1000 Torr.

The fluid pressure on a gas bubble is given by

$$P_{fluid} = \rho * g * h + pressure\ head\ above\ liquid\ ,$$

(4.4)

where ϱ is the fluid density (1 g/cm^3); g, the acceleration due to gravity; and h, the height of the fluid above the bubble. All bubbles were held approximately 3 cm below the surface of the water in all experiments performed in the bubble levitation cell; therefore, the fluid pressure term for all bubbles is roughly 2.21 Torr plus the pressure above the liquid, taken to be 762.8 Torr, the average barometric pressure of Ann Arbor, Michigan, over the course of the experimental

[33] A bubble that has $R_1 \neq R_2$ is a non-spherical bubble, i.e., ellipsoid in shape.

campaign. Therefore, the total pressure experienced by the bubble investigated here is just over atmospheric pressure, at roughly 766 Torr

It is worth noting that barometric pressure can have a large variation, much larger than the fluid pressure contribution due to depth (for depths used, 3 cm) or pressure due to surface tension (for considered bubble size). In the extreme case, record-breaking barometric pressures for the Ann Arbor area demonstrate the atmospheric pressure can vary between 718.8 Torr and 788.42 Torr. Using these values in the breakdown curve adjusts the pd minimum from 73.6 Torr-cm (from atmosphere as 762.8 Torr) down to 69.4 Torr-cm (from the 718.8 Torr case) and up to 76.1 Torr-cm (from the 788.42 Torr case). While these record pressures are on the periphery of typical experimental conditions, care should be taken during the experimental process to take into account the change in atmospheric conditions if during extreme weather.

4.3.2 Applied Breakdown Voltage Scaling versus Bubble Size

The results from both electrode configurations are shown in Figure 4.9 on the next page. Here, the applied voltage necessary to achieve breakdown is plotted against *pd*, where p is the total pressure within the bubble and d is the bubble diameter. Bubble position varied between 0.05 and 0.6 mm in the pin to plane geometry. In the plane to plane electrode configuration the bubble was located at the surface of high voltage electrode. These data show good correlation between the electrode types.

These data resemble a Paschen-like curve, with a minimum occurring around 10.1 kV with a pd value of 73.6 Torr-cm (Figure 4.9). The peak field at the Paschen minimum on the bubble surface was calculated (via *ANSYS Maxwell*) and found to be 370 kV/cm, well above the breakdown requirement for air (~30 kV/cm). While no breakdown data of air bubbles in water currently exists in the literature, comparisons to breakdown curves of air and water vapor may be made (see Figure 4.10). As can be seen in the figure, the Paschen minimum for the gas bubble occurs at a substantially higher pd. The large horizontal error bars are due to the uncertainty associated with measuring the bubble size.

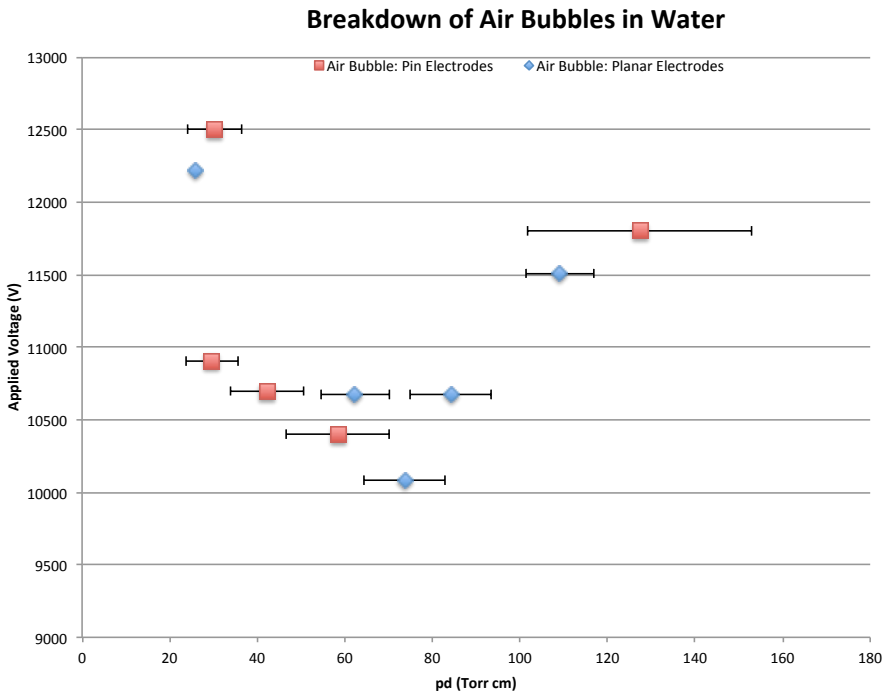

Figure 4.9: Breakdown curve of air bubbles in liquid water. Red square, pin-to-plane electrode results. Blue diamond, plane-to-plane electrode results. Error bars included on all points for pd error.

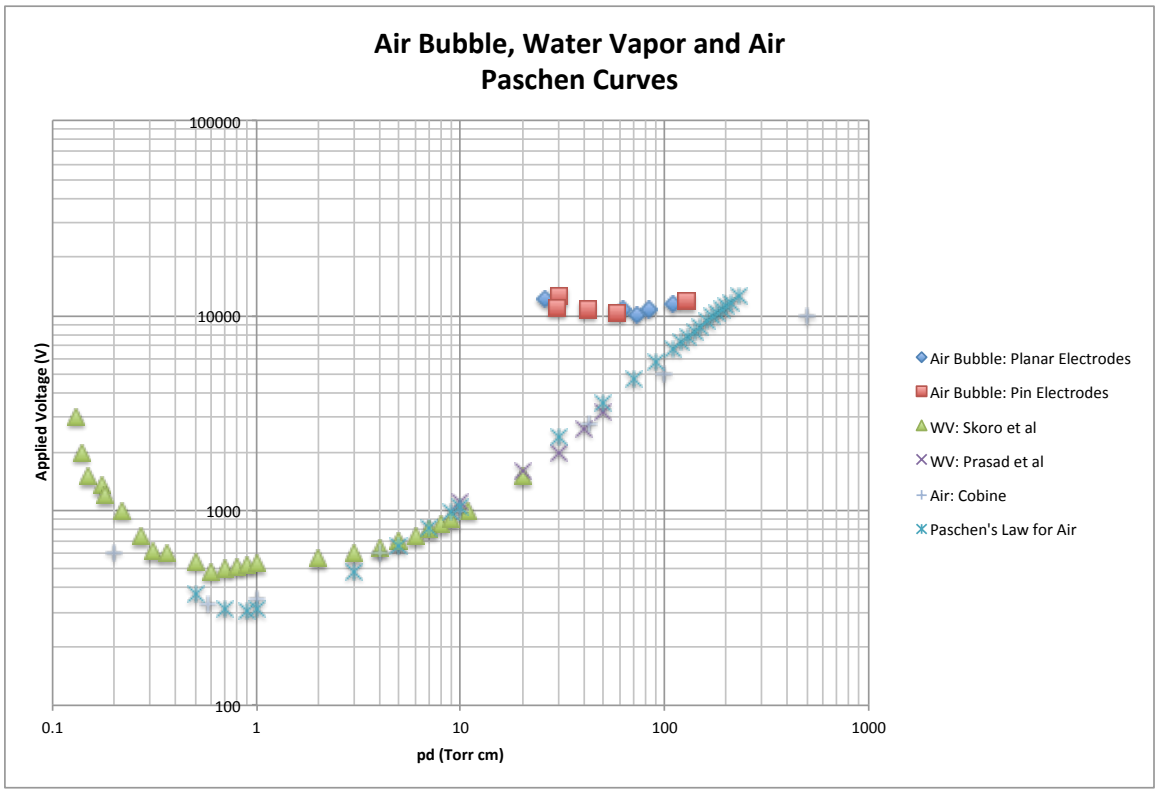

Figure 4.10: Breakdown curves: air bubble, water vapor [336,337] and air [338,339,340] (air breakdown curve includes values solved from Paschen's law).

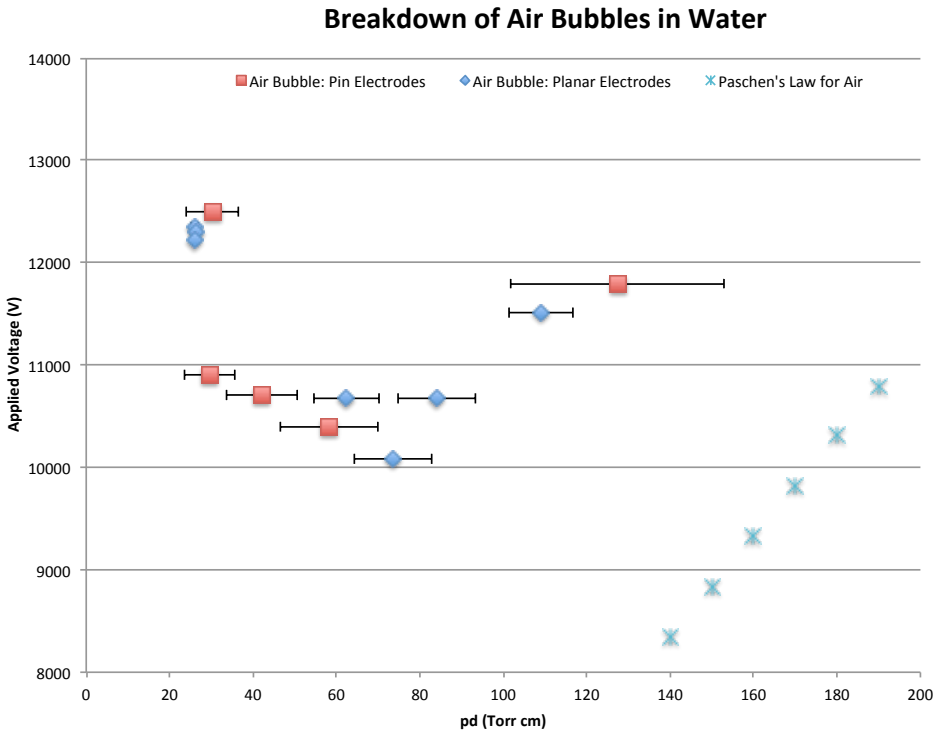

Figure 4.11: Close up of air bubble breakdown with Paschen's law scaling for air breakdown.

4.3.2.1 High pd Side of the Breakdown Curve

To the right of the apparent minimum, the air bubble breakdown curve appears to roughly correlate with Paschen's law for dry air (see Figure 4.11). This essentially linear behavior with pd is an especially interesting result, as breakdown of an air bubble immersed in water proceeds differently from breakdown in a low pressure gap with a uniform electric field. For example, for low pressure breakdown between electrodes where the electric field is uniform, the breakdown voltage is (see further discussion in Chapter 2):

$$V_b = \frac{Bpd}{\ln Apd - \ln\left(\ln\left(1 + \frac{1}{\gamma_{se}}\right)\right)} \tag{4.5}$$

Two characteristics that differ bubble breakdown from Townsend (and therefore Paschen-like) discharges are outlined.

1. *Electrode processes.* In dc breakdown, the Townsend ionization coefficient, α, is used to describe a cathode-emitted primary electron's ability to ionize neutral particles, creating more ion-electron pairs. However, in the air bubble in liquid water system, the streamer

essentially behaves as an extension of the electrode, and the construct of an ionization coefficient in the strictest sense loses that meaning.

2. *Secondary electron emission*. Key to Paschen's law and breakdown is the role of secondary electron emission, γ at the cathode. Breakdown occurs when

$$\alpha d = \ln\left(1 + \frac{1}{\gamma_{se}}\right). \quad \textbf{(4.6)}$$

In the case of a bubble, the liquid interface would be the emission surface. However, the secondary electron emission coefficient of water (~2×10^{-4}, γ of water surface [**341**]) is quite small. For an air bubble of 1 mm in diameter, (4.6 requires α to be more than 8500 cm^{-1}. Field-driven processes (e.g., field emission, tunneling, etc.) are believed play the role of ion induced secondary emission at the interface , especially for cathodic streamers [**328**]. These data suggest the need to elucidate the secondary emission of water-gas mixtures or – and perhaps more accurately – uncover the new physics that plays the role of traditional secondary emission in these mixed phases of matter.

4.3.2.2 Low pd Side of Breakdown Curve

Voltage required to breakdown smaller bubbles increases rapidly with decreasing diameter. The rapid rise is a consequence of the fact that for small bubbles, the integrated ionization product (ionization coefficient*dx) is too low for streamer formation in small bubbles, at least over the E/N values explored in this work [**107**]. Simulations by Babaeva and Kushner [**114**] investigated the breakdown of series of bubbles smaller than those considered here (10 – 35 μm). It was found that bubbles with properties within the Paschen breakdown regime for air developed stronger and faster streamers versus those below the Paschen curve.

While additional physics are expected to come into play due to the nature of the bubbles in liquids, those results suggest the low pd side of the curve shown in Figure 4.9 may be the result of external effects. Possible variables that would affect the breakdown curve include distance from electrode, liquid conductivity and temperature-[**329**,**107**]. However, further experiments are necessary to determine if this is the true physical behavior of the system or an artifact of the experimental process via charging. For both single and multiple bubbles for both electrode configurations investigated (i.e., pin-to-plane and planar), the charging of these bubbles due to the electric fields of high voltage pulses can prevent breakdown.

4.4 Bubble Charging

Experimental observations associated with bubble motion subsequent to the voltage pulse suggest the possibility of bubble charging. In this case, the interface would be charged. The interaction of the interface with the applied field would give rise to a force on the bubble. Such a force could conceivable displace the bubble from an electrode. The deposited charge could also weaken the field inside the bubble, thereby reducing the likelihood of breakdown. This charging can be significant enough to induce kinetic motion of the bubble (see Figure 4.16) as well as prevent breakdown at values of applied voltage that induced breakdown previously (see Figure 4.18 through Figure 4.20). This latter consideration would modify the breakdown curve. Data presented later suggests that charging effects can increase the breakdown voltage by as much as nearly 15%.

Korobonikov et al. asserts that this charging is important in the development of underwater breakdown channels, hypothesizing that the field due to deposited charges, as they spread throughout the interior of the bubble, would prevent avalanches from forming into a streamer "even under the effect of the total pulse amplitude" [**250**].

In addition to the induced charge (charge deposited on the surface of a bubble from the applied electric field), charging of bubbles – and on literally all particles in liquids – does naturally occur. The hypothesis formed in this work to understand the assumed charging observed is motivated from this natural occurrence of charge, the zeta potential. A naturally occurring analogue is believed to provide a narrative on the mechanisms and implications of an induced charge.

4.4.1 The Zeta Potential

All particles in liquids develop a net charge at the interface between the bulk liquid and the particle. The particle acquires a surface charge due to sorbtion of liquid ions to the particle, the particle chemistry, and/or particle surface potential. The potential produced by this surface charge is commonly referred to as the Stern layer. This layer then attracts oppositely charged ions that shield out the particle's surface charge from the rest of the liquid. This diffuse layer is the particle equivalent of the Debye length in plasmas (indeed, the electrical double layer structure of particles in liquids is also referred to as the "Debye layer"). Beyond this layer the

charge effects on the particle are shielded out and the liquid is essentially neutral, as in the analogous plasma (refer to Figure 4.12 for a diagram).

$$\lambda_D = \sqrt{\frac{\varepsilon\varepsilon_0 k_B T}{2C_{salt}e^2}} \quad \textbf{(4.7)}$$

As an example of the Deybe length in a liquid solution with colloids, (4.7 is the Debye length for a monovalent salt solution (e.g., NaCl, KCl, etc.), where C_{salt} is the salt concentration (mol/L) and the other variables are standard thermodynamic variables [**342**].

Within the diffuse layer is a stable boundary, where the potential at this boundary remains constant as the particles moves throughout the liquid. This potential is referred to as the zeta potential (also referred to as simply ”ζ” in colloidal science literature) [**343**].

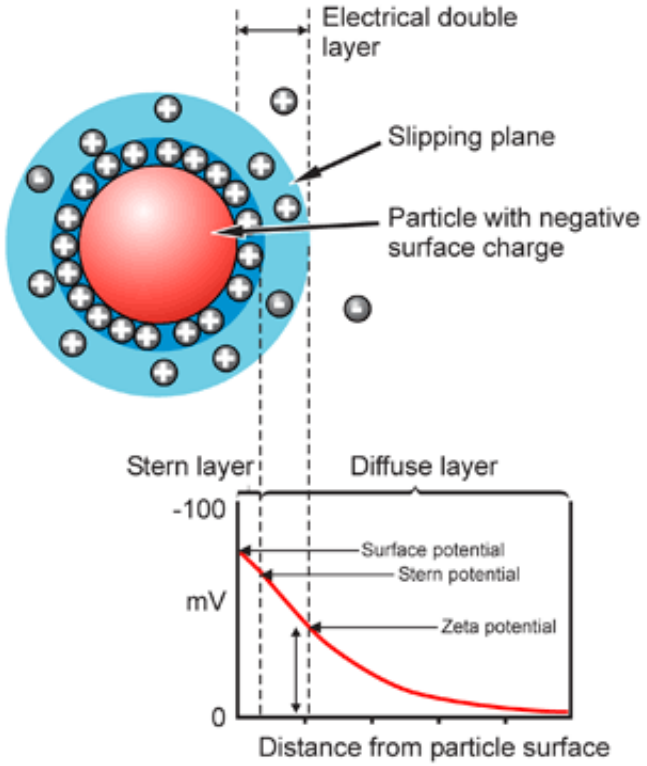

Figure 4.12: The electrical double layer of a particle in a liquid suspension. From [344].

4.4.1.1 Zeta Potential of Air Bubbles in Water

It is well established that the surface of an air bubble submerged in liquid water will charge negatively (beginning with Quincke in 1861 [**345**]); in pure water this is due to the dipole

orientation OH^- ions [**346**]. In 1995, the zeta-potential (ζ) of air bubbles in deionized water was first determined to be -65 mV [**347**], though this value will fluctuate depending on the composition of the liquid [**348**] (e.g., pH); today, abundant research has been dedicated to determining the zeta-potential of a host of various colloids and bubbles in various liquids (e.g., [**349**]). Beattie et al. [**350**] demonstrate that water strongly sorbs hydroxide ions, and this is only counteracted at pH of 2 through 4 (i.e., the isoelectric point for air bubbles) – which, it must be pointed out, air plasmas do produce. As mentioned above, almost no application of the zeta potential or additional charging has been applied to plasmas in liquids.

4.4.2 Upper limit of bubble charge

The theoretical upper limit of bubble charging may be calculated. When the electrostatic pressure on the bubble surface is greater than the surface tension on the bubble, the bubble will be affected. Analysis of the charge required to overcome the surface tension on the bubble reveals an upper limit of the charge that a bubble may carry.

As discussed in the previous section, the Young-Laplace equation describes the pressure differential across the interface between two immiscible fluids (e.g., the interface of a gas bubble in its liquid environment). For a sphere of radius R, the additional pressure is given by (4.3) (repeated here):

$$\Delta P = \frac{2\gamma}{R}.$$

(4.3) (repeated)

F_{ES} is the force due to the electrostatic pressure on a sphere with surface charge q.

$$F_{ES} = \frac{\varepsilon_0}{2} 2\pi R^2 \frac{q^2}{(4\pi\varepsilon_0 R^2)^2} \int_0^{\pi/2} \cos\theta \sin\theta \, d\theta \; = \frac{q^2}{32\,\pi\varepsilon_0 R^2}$$

(4.8)

Electrostatic pressure on a bubble is given as

$$P_{ES} = \frac{F_{ES}}{Area}$$

(4.9)

$$\frac{F_{ES}}{Area} = \frac{q^2}{32\,\pi\varepsilon_0 R^2} \times \frac{1}{\pi R^2} = \frac{q^2}{32\,\pi^2\varepsilon_0 R^4}$$

(4.10)

From (4.3) and (4.10), the inequality then becomes

$$\frac{q^2}{32\,\pi^2\varepsilon_0 R^4} > \frac{2\gamma}{R}$$

(4.11)

or

$$|q| > \sqrt{64\,\gamma\,\pi^2\varepsilon_0 R^3}$$

(4.12)

Substituting in the applicable values, the upper limit of the surface charge that can be applied to the bubble surface is given in the following plot below (see Figure 4.13). Maximum charge is plotted for several water temperatures, as the surface tension of water depends on temperature.

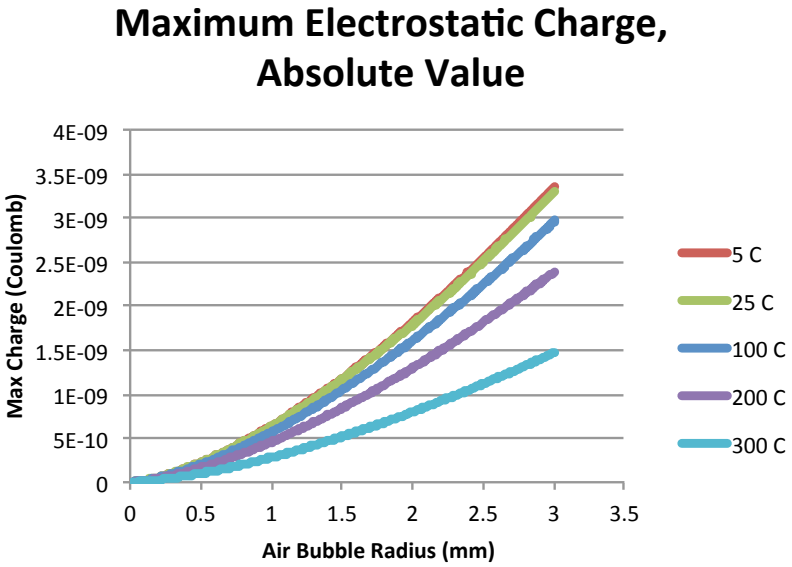

Figure 4.13: Absolute value of the maximum electrostatic charge an air bubble may withstand before the surface tension of the bubble is affected. Plotted for various temperatures of water.

Solving for the potential developed by the maximum charge via (4.13),

$$V = \frac{q}{4\pi\varepsilon_0 R},$$

(4.13)

the maximum potential that an air bubble may theoretically hold is determined and plotted in Figure 4.14.

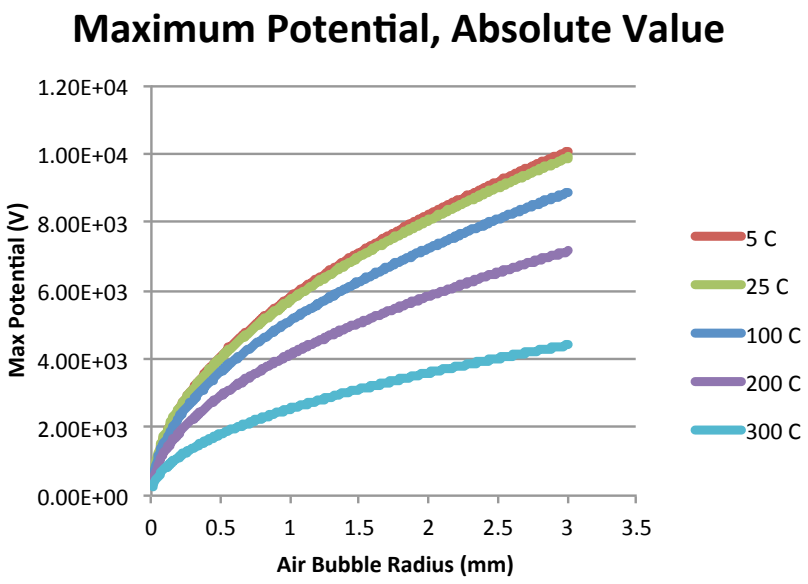

Figure 4.14: The theoretical limit of the absolute value of the maximum potential that an air bubble is able to sustain.

The results in Figure 4.14 are important as they provide a guideline as to how much a bubble may theoretically withstand breakdown from an applied field; i.e., how much of a larger potential hill the applied field would have to overcome to initiate breakdown in the bubble. At the very least, it acts as a check on the results shown in Figure 4.20, in which one of the bubbles required an additional 1.55 kV to breakdown to overcome the charge effect. From Figure 4.14, the theoretical limit of charge a bubble of radius 0.5 mm can support is just over 4 kV, generously accommodating the additional holdoff voltage observed in Figure 4.20. The calculations show an air bubble may theoretically sustain several kilovolts of potential. Computational results of the effect of such possible potentials on air bubbles may be found in the following section.

4.4.2.1 Electromagnetics and Charged Air Bubbles

The effect of various potentials on air bubbles was modeled with *ANSYS Maxwell*, as seen in Figure 4.15.a-d. This finite element method electromagnetic field solver was used to calculate the electric field produced by the electrodes. The bubble shown in Figure 4.15.a-d was a replicated scenario of a bubble in which plasma was produced (shown in Figure 4.15.e). The high voltage needle electrode was biased at +10.7 kV to replicate the experiment in which plasma was generated within the bubble. A summary of the results may be found in Table 4.2.

It is seen that the effect of including a minor potential (bubble (b), -65 mV, the zeta potential of air bubbles in deionized water [**347**]) has a strong result on the Meek criterion or ionization product *M*, where *M* of approximately 20 is required to form streamers (refer to (2.24)).

Figure 4.15: Simulated effect of charge on air bubble (a – d); experimental production of plasma in bubble (d). Electric fields for effect of HV needle electrode at +10.7 kV.

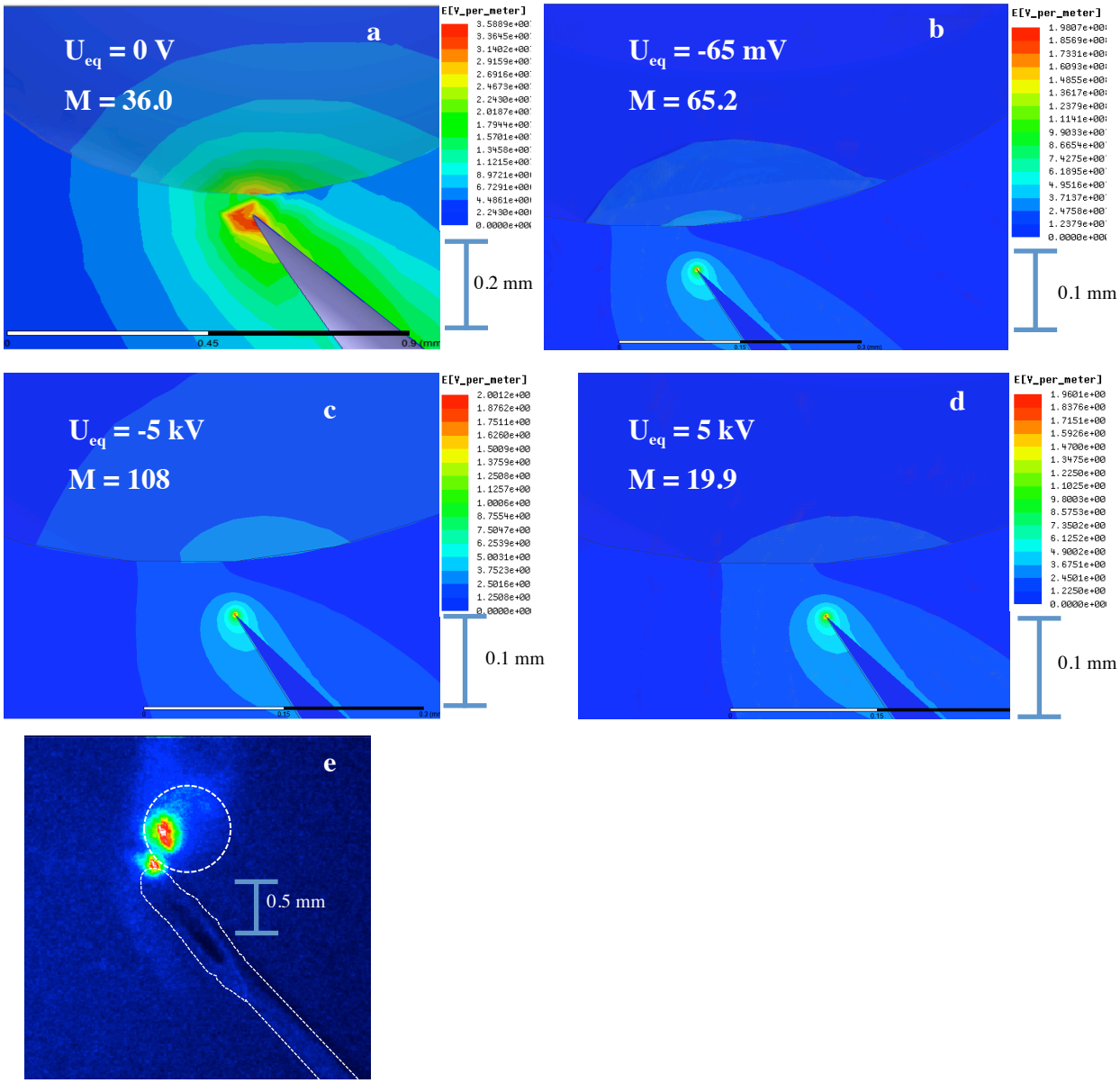

Using a theoretical upper limit of charge, equivalent to a potential of -5 kV, as seen in bubble (c), *M* increases to over 100. However, if the bubble carries the same charge but of positive polarity, as in bubble (d), the Meek criterion sinks to approximately 20. As this is near the criterion it is possible that no breakdown will be sustained. It is important to note that the bubble simulated in Figure 4.15 is a very promising candidate for plasma ignition due to its close

proximity to the electrode. It is equally important to note that *M* is given as an estimate value (as seen in (2.24) and not a rigid limit. Regardless, the data suggest the presence of a charge on the bubble (albeit an extreme, at the theoretical maximum) would allow the bubble to resist breakdown.

It is important to indicate these results are the product of an electromagnetic solver that most likely does not reflect the true nature of water and electrical discharges. At the very least, these results suggest simulation of electrical discharges in liquids should include additional variables not previously considered.

Table 4.2: Effect of various electric potentials on air bubbles. Results of simulation.

no.	**Charge on Bubble**	**Equivalent Potential**	**Highest Electric Field at Bubble**		***M*, Ionization Product**
	C	*V*	*kV/m*	*Td*	
a	None	None	3.25×10^{2}	1.30×10^{3}	36.0
b	-7.23×10^{-15}	6.5×10^{-2}	3.09×10^{2}	1.24×10^{3}	65.2
c	-4.29×10^{-10}	-5×10^{3}	3.12×10^{2}	1.25×10^{3}	1.08×10^{2}
d	4.29×10^{10}	5×10^{3}	1.84×10^{2}	7.34×10^{2}	19.9

4.4.3 Effects of Charging on Bubble Breakdown

Two effects attributed to bubble charging have been observed. The first is induced kinetic motion of the bubble, where the bubble appears to move to and from the immediate electrode region. This displacement is believed to be due to the repulsion of space charge from the applied voltage pulse and can occur over distances as large as ~1 cm. The second effect observed in this wok also supports the charging effect is an increase in holdoff voltage required to breakdown a bubble. Both phenomena are observed in both attached and unattached bubbles. Both phenomena, especially the occurrence of kinetic motion, appear to require several non-plasma producing pulses to develop.

4.4.3.1 Kinetic motion

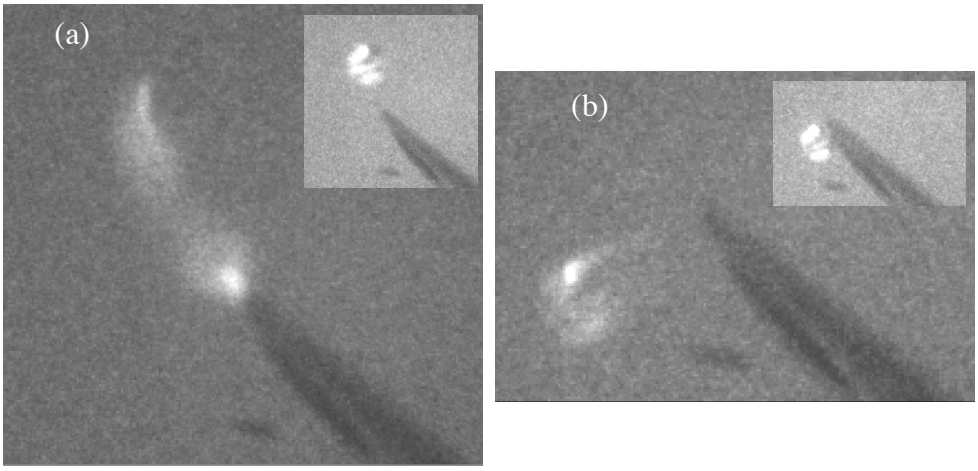

Figure 4.16: Various images of air bubbles popping on and off the electrode. Small image in upper right is of bubble before pulse.

As seen in Figure 4.16, after subjection to several (5+) pulses that do not produce plasma (such as ramping up to breakdown voltage), bubbles may undergo a brief (less than the exposure time of the system, > 5 ms), jumping motion during the application of high voltage pulse (see Figure 4.9 for typical voltage trace). This kinetic motion is believed to be due to the attraction or repulsion of the bubble due to the accumulated charge (charge originating from previous pulses). Due to the nature of bubble charging as it is currently understood (i.e., the zeta potential), the charge on the bubble may be either negative or positive, and is strongly affected by the concentration of H^+ and OH^- ions at the bubble interface [**349**]. Plasma discharges in water are excellent sources of both ions. Indeed, the understanding of the role of natural charging (i.e., the zeta potential) is poorly developed; in an environment where the bubble is subjected to fast-rise time (here, 100 ns) high voltage pulses, further experimentation that is beyond the scope of this dissertation is required. However, observations and theories to explain this phenomenon are outlined.

This kinetic motion of the bubble is believed to be due to an increase in negative charge on the bubble surface from the positive peak of the high voltage pulse. The electric field produced by the positive high voltage pulse then attracts negative species toward the field-side of the bubble. As seen in Figure 4.16.a, this may be strong enough to draw the bubble to the electrode. Alternatively, as in Figure 4.16.b, the bubble carrying this strong negative charge may be then repulsed by the electric field produced by the negative high voltage undershoot (see Figure 3.5

for typical voltage pulse). As the field dies away, the bubble is pulled back to its initial position via the acoustic pressure field.

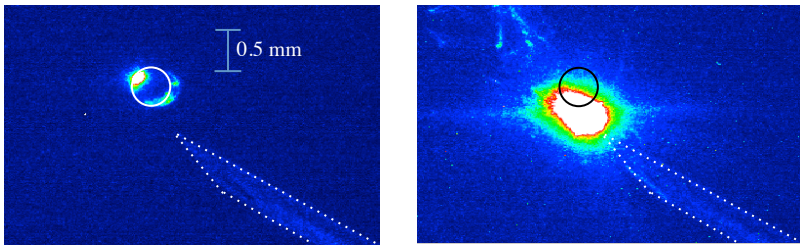

Figure 4.17: Bubble contortion due to believed charge-induced motion. Left, before high voltage. Right, breakdown in the bubble at 12.1 kV, original bubble placement and shape indicated by the black circle.

This phenomenon may also be observed in bubbles that both are drawn toward the electrode and are ignited with plasma. As seen in Figure 4.17, breakdown is induced from a pulse of amplitude 12.1 kV in a bubble of diameter 0.46 mm. The contortion of the motion is observed on the bubble shape. The bubble is originally 0.39 mm away from the electrode before the pulse and is drawn to the electrode tip. Based on the time scales of the images (exposure time of 5 ms), the bubble experiences a minimum acceleration of 31 m/s^2.

4.4.3.2 Charging resulting in increased breakdown voltage

Beyond simply displacing the bubble from the region of high field, charging can also play a role in suppressing the field in the bubble, implying that charged bubbles can be more difficult to breakdown. A similar field shielding effect was observed by Wetz and colleagues [**351**]. In that study, they found that field-emitted electrons in vapor bubbles near the powered electrode increased the hold-off ability of the water. Their simulations of an electrode with an effective electric field of 45 MV/cm at the tip was decreased to between 20 and 35 MV/cm when a simulated r = 2.1 μm bubble charged with 1.76×10^{-10} C was attached to the tip. (It should be noted that this amount of charge is not actually physically capable of being applied to a bubble – the largest charge a bubble of this size at 25 °C could carry before rupturing under the electrostatic forces is only 6.1×10^{-14} C (discussion on maximum charge carried by a bubble in the following section).)

Figure 4.18 illustrates bubble charging and the increased hold-off effect with a single bubble powered by planar electrodes. Here, the bubble's buoyancy rests the bubble on the top high voltage electrode. The images shown in Figure 4.18 depict the result of charging on the bubble and the inability to ignite plasma within the bubble at voltages higher than V_{br}, where V_{br} is the

lowest voltage necessary to produce plasma (here, V_{br} = 12.22 kV). If charging is the underlying reason for the increased hold-off voltage, it suggests charge from previous breakdown is not only important but also long lived (i.e., seconds time scale). Electrons do not move quickly in water; Zahn et al. [**352**] give the mobility of electrons in water as $2x10^{-7}$ $m^2/V*s$, though more experimental progress needs to be made to address this question of charge diffusion in water.

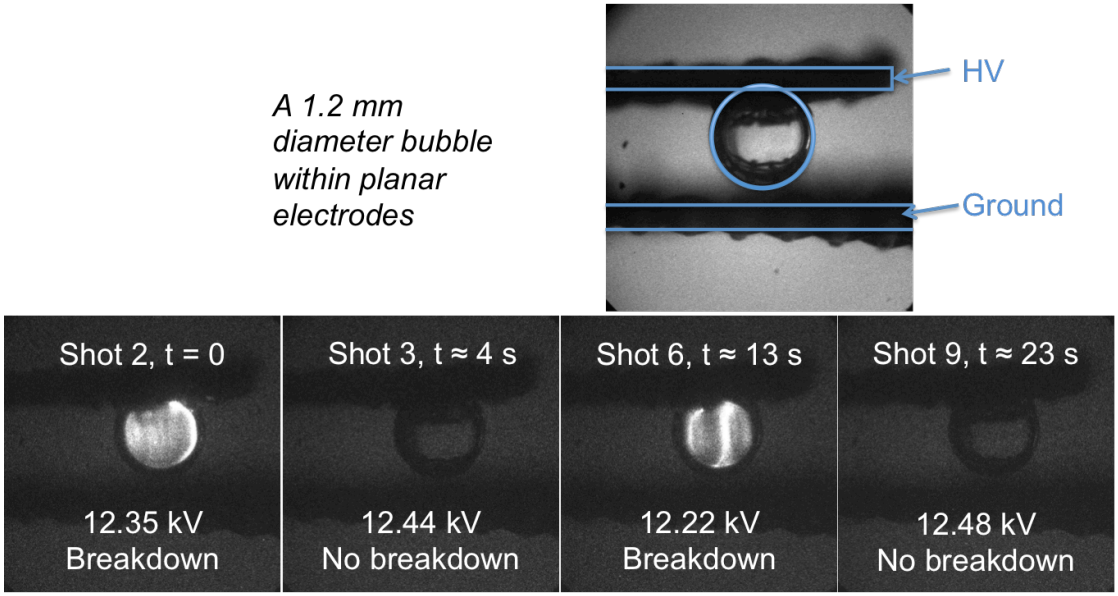

Figure 4.18: A single air bubble (1.2 mm diameter) between planar electrodes. The bubble resists breakdown over long periods of time.

This phenomenon was observed with levitated bubbles in the pin to plane configuration as well. In Figure 4.19, plasma is induced in an air bubble of 1.24 mm diameter at 13.0 kV. Sixteen succeeding pulses of various amplitudes between 13.0 to 13.8 kV were applied 15 to 30 seconds apart resulting in merely a faint glow at the electrode tip or no observable emission. The eighteenth pulse resulted in breakdown at 13.6 kV, the same or lower voltages as previously applied pulses.

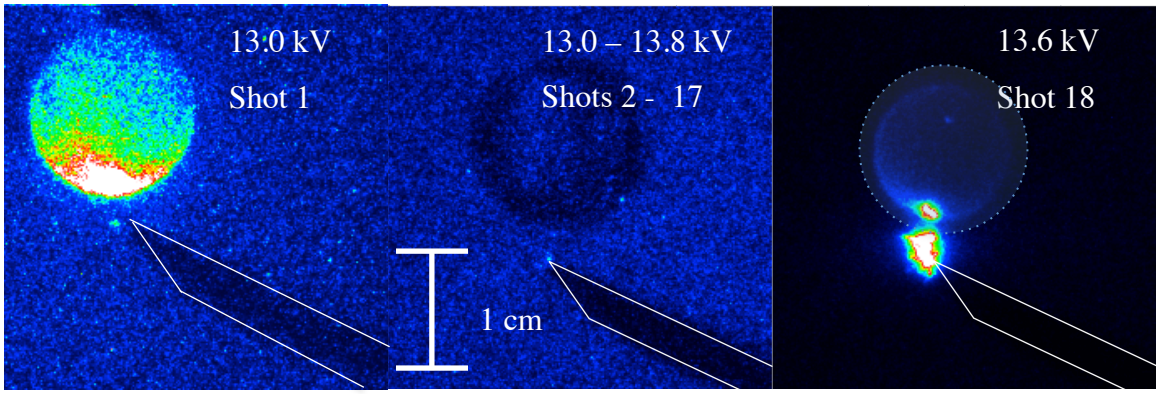

Figure 4.19: Evidence of increased hold off voltage in point to plane electrode configuration. Air bubble, 1.24 mm diameter. Left image: plasma induced in bubble at 13.0 kV (left). Middle image: subsequent multiple HV pulses (13.0 – 13.8 kV) separated by tens of seconds between pulses produced emission shown (faint glow at tip) or no emission. Right image: Plasma produced at 13.6 kV.

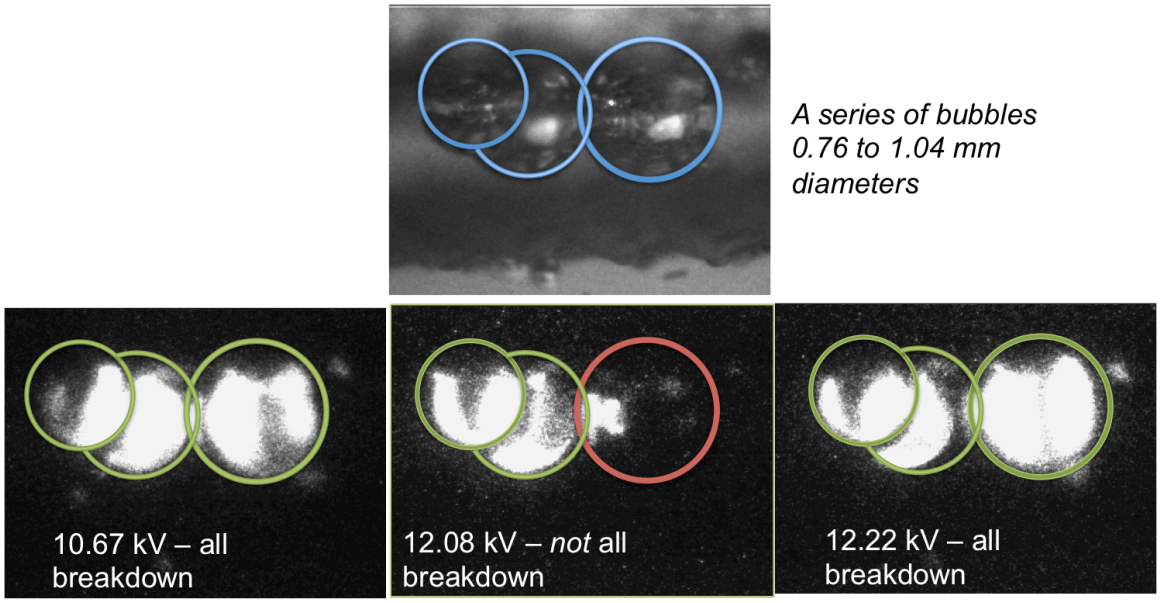

Figure 4.20: Bubble charging in multiple bubbles and the prevention of breakdown.

As seen in Figure 4.20, a group of three bubbles of 0.76 mm to 1.04 mm in diameter is deposited on the surface of the planar mesh electrode. Plasma is ignited in all three at an applied voltage of 10.67 kV. However, this voltage is inadequate to breakdown the bubbles at subsequent application of voltage pulse. In fact even at a considerably larger voltage of 12.08 kV, only two of the three bubbles experience breakdown. All three bubbles breakdown at 12.22 kV. An additional 1.55 kV is required to breakdown the third bubble. The fact that not all bubbles responded to the voltage pulse in the same manner suggests that discharge intensity at the initial breakdown where plasma was formed in all bubbles was not the same. This would

imply that surface charge for each bubble is likely different, or that diffusion of charge from the bubble to the surrounding water is nonlinear.

4.4.3.3 Discharge Propagation External to Bubble

In addition, breakdown has been observed to occur with the discharge completely avoiding the bubbles (see Figure 4.21).

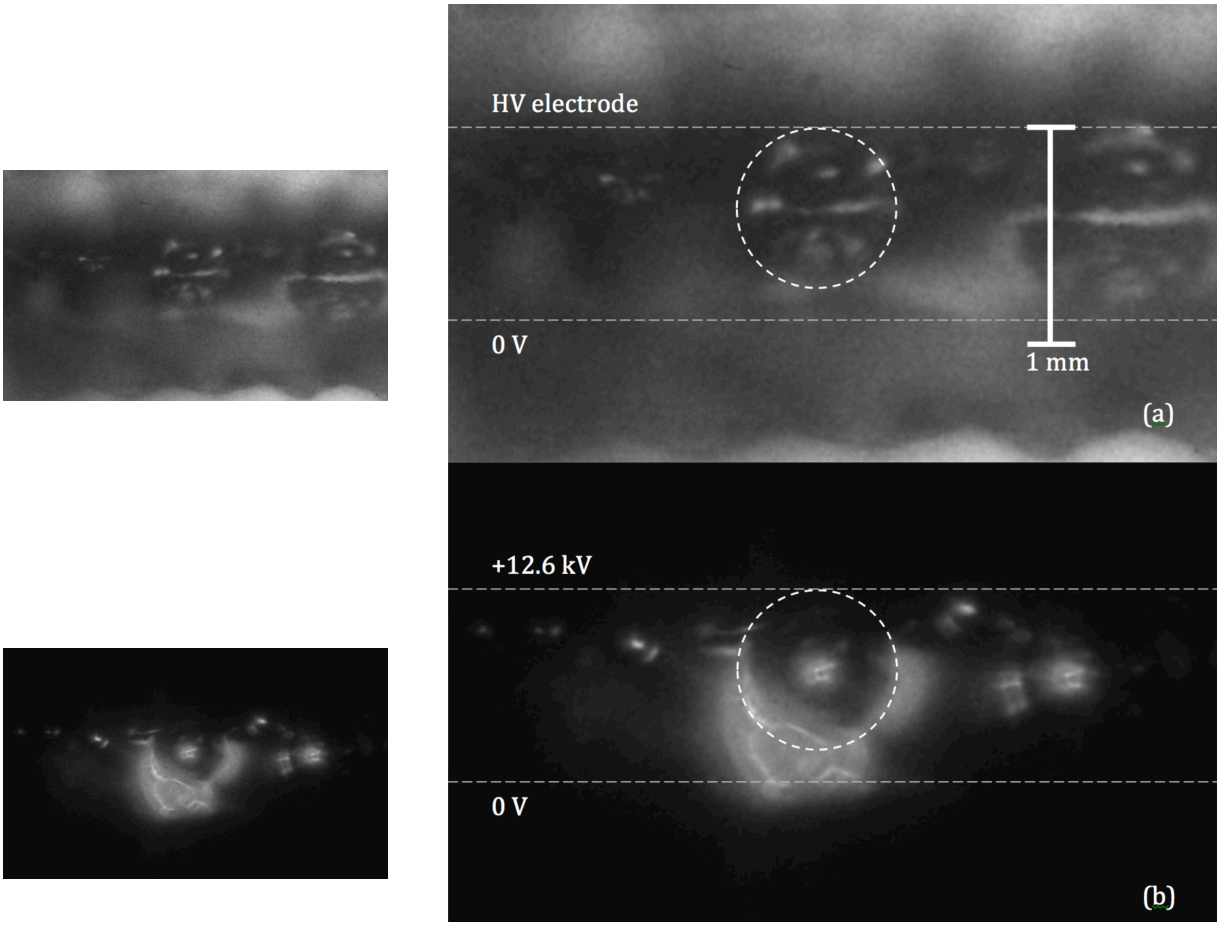

Figure 4.21: (a) Air bubbles and planar electrodes, electrodes at approximately 0.9 mm gap. (b) Discharge between electrodes, arcing around bubble.

Here, the discharge is observed to occur along the bubble water interface, external to the bubble. This observation is interesting in that published streamer in bubble studies suggest that the discharge propagates along the *inner* surface of the bubble, not external [**332**]. These data show that external propagation of the streamer ultimately propagating as a liquid streamer that reaches the ground electrode. In this case, the presence of the dielectric discontinuity at the interface along with potential charging of the interface could not only locally amplify the electric field at the interface, but also guide the discharge around the curved surface of the bubble as

observed here. This is not an insignificant result, especially for those concerned with avoiding arcs during high field applications in liquids; this result is relevant for pulsed electric field (PEF) technology for food processing [**353**]. Awareness of such possible charging leading to undesirable arcing is necessary to create functional high-field technology.

4.4.4 Consequences and Closing Thoughts

Bubble charging effects may have implications in multiple fields, such as plasma medicine. Most cellular membranes are negative; therefore, the charge or resultant charge of a bubble (from dissolved gases) will also dictate the permeability of the plasma treated liquid to the cell wall. This characteristic is already being applied in nanotechnology and nanoparticle-based biological devices [**354**]. Further study between plasma discharges in liquids and the charging of bubbles proposed here is necessary to establish control keys not only for plasma medicine, but for all plasma in liquid applications.

In addition, based on the simulation results from Figure 4.15 and Table 4.2, bubbles that can resist breakdown may be positively charged. This is in comparison to the observed kinetic motion of bubbles, which suggest a negative charge is most likely. Naturally occurring charge on air bubbles has been measured to have potentials that range from roughly +20 mV to -120 mV. It may be possible that air bubbles subjected to electrical discharges have the ability to become very positively *or* negatively charged, depending on water composition, localized heating or conductivity changes, molecular orientations, and so on.

In this regard, interpretation of the breakdown curves, particularly for electrode attached bubbles, must be done so in the context with this potential charging process in mind, which would have the effect of adding some scatter, particularly if the same bubble is used for each point. One of the many aspects of this charging phenomenon that is not understood are the diffusion time scales of the charge; how much time required for excess charge to dissipate from a bubble does not appear to be constant.

Chapter 5:

The Gas-Liquid-Plasma System & Resultant Chemistry

5.1 Overview

The experimental apparatus described in Chapter 5 allows for the detailed study of discharge physics of bubbles in liquids. Because the ultimate goal of discharges in liquids studies is to engineer a plasma water purification system, the necessary next step beyond understanding the discharge physics is the associated chemistry induced or driven in the liquid medium. The apparatus used to trap and ignite single bubbles or small bubble ensembles has only limited utility in the study of actual chemistry for a number of reasons, namely:

1. Optical emission spectroscopy is difficult in the levitation cell (e.g., small discharges and very long optical path lengths through water, a significant UV absorber V [**355**]
2. Input power to a single bubble is small, resulting in only small changes in water chemistry. This requires highly sensitive diagnostics, some of which are, practically speaking, impossible to perform (i.e., nanograms- and picograms-per-liter, or parts-per-trillion and-quadrillion, respectively, of investigated species)

This chapter describes chemical studies driven by an underwater plasma jet. The effect of different operating conditions on plasma parameters is detailed, with the goal of identifying various control methods to create a discharge with desired properties. The use of the plasma jet on various aqueous contaminants is detailed. A large range of different contaminants is investigated, including a textile dye (methylene blue), halogenated compounds, and algae pond water. The cytotoxicity of plasma-purified methylene blue solutions is investigated.

5.2 Experimental Approach

The plasma-driven chemistry of the DBD jet discharge is examined with the device described in Chapter 3. Unless otherwise stated in the experiment description, the device is powered with a low-frequency ac voltage (5 kHz). Here, a high voltage electrode is surrounded by gas flow, and a ground electrode is coiled around the base of the gas tube. The high voltage electrode used was

composed of either tungsten or copper. The discharge occurs within an unsteady bubble formed at the exit of the submerged device in the liquid water. A variety of gases and gas mixtures were investigated (see Table 5.1).

5.3 Baseline Plasma Parameters

5.3.1 Plasma Properties

It should be noted that as the ultimate goal of this dissertation research is to develop the foundation for the development of a viable plasma-based water purification system, the preferred gas is room air or self-generated steam (see Chapter 6 for details on the steam discharge, not discussed in this chapter). For completeness sake, the basic parameters of plasma discharge with all four main gases and mixtures are presented in Table 5.1.

Table 5.1: Typical electron densities.

Plasma	Average Electron Density (m^{-3}, via H_α)	Gas Temperature (K)
Air	1×10^{21}	*Typical Range:* 1800-2500, up to 3000
Argon	1×10^{21}	
Helium	5×10^{20}	
Steam	1×10^{21}	
Argon + Helium	1×10^{21}	
Argon + Air	1×10^{21}	
Helium + Air	5×10^{20}	

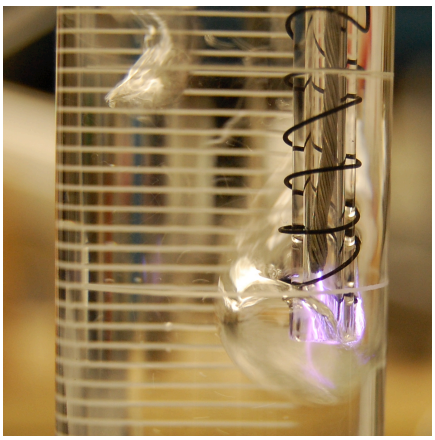

Figure 5.1: Plasma jet in liquid water with room air gas flow (2.36 SLPM flow rate). Copper is driven at high voltage.

5.3.2 Resulting Chemistry: pH and Conductivity

Air plasmas in water have been known to cause acidification in the treated liquids [**356**,**357**,**358**,**359**,**360**,**361**]. This change is primarily due to the formation of nitric and nitrous acids formed by the air plasma as a result of the interaction of reactive nitrogen species (RNS) with water [**362**]. This change (e.g., Figure 5.2) is logarithmic, and due to the acidic solution coming into equilibrium. The conductivity of the solution also increases. This is due to a variety of factors, including electrode etching/removal through electrolytic processes and production of ions in solution (e.g., hydrogen ion concentration increases as the solution becomes more acidic, as in [**357**]). Figure 5.2 illustrates this characteristic pH and conductivity behavior of air discharges in liquid water.

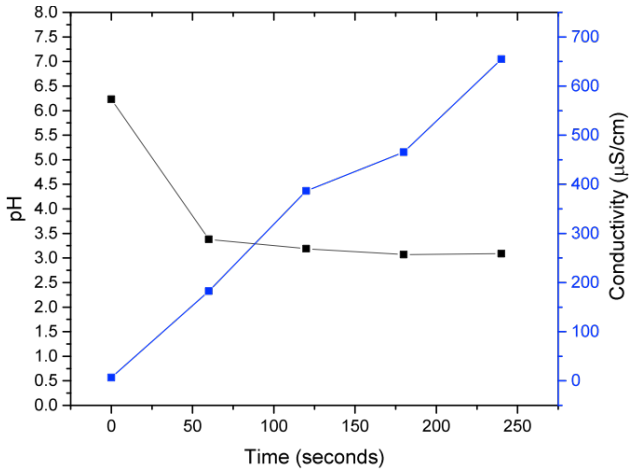

Figure 5.2: Change in pH and conductivity for a humid air plasma jet in deionized water (2.36 SLPM gas flow).

5.3.2.1 pH

In Figure 5.2 above, the saturation of the pH curve is related to the various plasma-produced acids in solution coming into equilibrium. The strength of the acid (the dissociation constant) determines the amount of water the acid can ionize. Using the Brønsted theory of acids[34], in which the acid is defined as a proton (H^+) donor and a base, a proton acceptor, equilibrium of acid dissociation is given as

$$HA \rightleftharpoons A^- + H^+ \quad (5.1)$$

[34] N.b., in contrast to the Lewis theory of acids, in which an acid is defined as an electron acceptor and a base an electron donor.

In (5.1, HA represents the acid; A^-, the conjugate base of the acid; and H^+, the acidic hydrogen. The dissociation constant, K_a, is a quantitative measure of acid strength. K_a of the reaction in (5.1 is determined from the concentrations (in mol/L, or M, molarity) of the reaction in equilibrium, and is given by

$$K_a = \frac{[A^-][H^+]}{[HA]}$$

(5.2)

Due to the magnitude of K_a values, pK_a (similarly to pH or pOH, is equal to $-\log_{10}(K_a)$) is generally used[35]. Large values of pK_a indicate weak acids, and strong acids by definition have pK_a values of less than -1.74, which is the pK_a value for the hydronium ion (H_3O^+).

5.3.2.1.1 Acid Determination via pK_a Curve

Plasma discharges in air and water result in complex mixtures of molecular species (e.g., [**357**,**73**]). A titration curve was completed to investigate the acid composition via pK_a determination (Figure 5.3). By taking the log, base ten, of both sides of (5.2, and recognizing that $-\log_{10}(K_a)$ and $-\log_{10}(H^+)$ equal pK_a and pH, respectively, one arrives at the Henderson-Hasselbalch equation:

$$\mathrm{pH} = \mathrm{p}K_a + \log_{10}\left(\frac{[A^-]}{[HA]}\right)$$

(5.3)

During a titration, when the solution is half neutralized, the concentration of conjugate base of the acid equals the concentration of the acid. This leads the logarithm term on the right hand side of the equation to equal zero ($\log_{10}(1) = 0$), and the pH of the equivalence point equals[36] the pK_a of the acid.

The curve in Figure 5.3 was produced via a potentiometric titration of 0.1% NH_4OH with 100 mL of deionized water that was treated with an air plasma for 55 minutes. The plasma-processed liquid was measured to have a pH of 2.15 and a conductivity of 2010 μS/cm at the beginning of the titration.

[35] E.g., for H_2O, $K_a = 1.8\times10^{-16}$; pK_a = 15.7.
[36] Equality is numerical, as pH and pK_a are unitless.

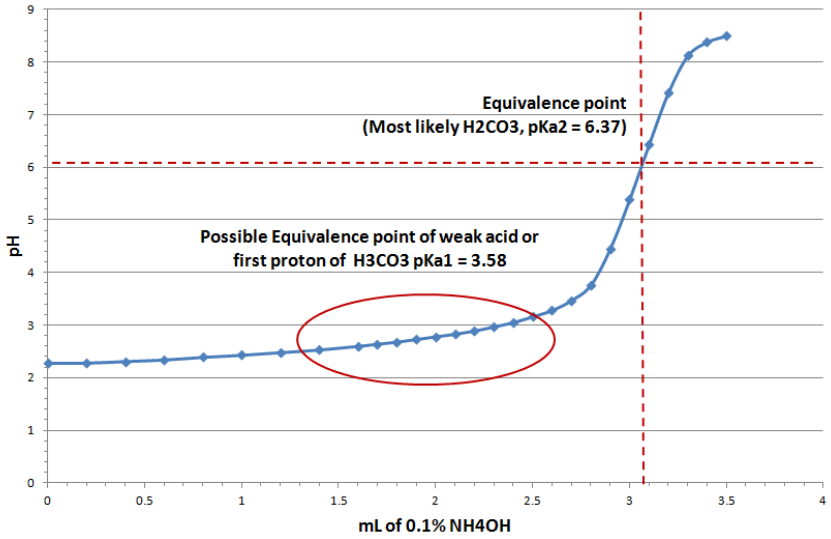

Figure 5.3: Titration of air plasma treated water with NH_4OH to determine acid composition.

The results of the titration suggest one of the acids present in the plasma treated water is H_2CO_3. This is indicated by the second proton dissociation[37] or location of the second equivalence point, $pK_{a2,}$ at 6.37 [**363**]. The data suggest there may also be an additional equivalence point with a pK_a around 3.58, which can also indicate H_2CO_3 [**363**]. Mixtures of acids are best determined with this method if their K_a values are three to four orders of magnitude in difference [**364**], meaning it would also be possible to detect HNO_3 (nitric acid, pK_a = -1.3 [**363**]) upon the repeat of the experiment. One possible method of determining the composition of the mixture of acids produced in plasma treated water is NMR titration (e.g., [**365**]), which is a direct method of determining protonation of compounds present.

5.3.2.2 Conductivity

The conductivity curve in Figure 5.2 is usually understood as a result of the acidification of the liquid, as conductivity measurements are sensitive to the concentrations of hydrogen [**357**]. However, as seen in Chapter 6, the steam discharge, which does not appreciably raise pH, also increases in conductivity. Therefore, a more correct explanation of increasing conductivity in plasma discharges in water is believed to be due to the formation of H_3O^+. As the acids come into equilibrium within the treated water, the presence of H^+ does not necessarily equal a reduction in

[37] H_2CO_3 is a diprotic acid, meaning it has two acidic hydrogen atoms. Acids are assumed to undergo stepwise dissociation, meaning the molecule loses an acidic hydrogen at a time. Each acidic hydrogen has its own K_a (K_{a1}, K_{a2}, etc.).

pH. The nuance behind this definition stems from the equilibrium of acid dissociation, as discussed previously.

5.4 Time Averaged Studies

To understand the induced chemistry in the liquid phase driven by plasma exposure the time evolution of the DBD jet plasma properties were measured. Time averaged studies were conducted with the monochrometer discussed in Chapter 3. The plasma jet may be operated with many gases[38] though only argon, helium (all > 99.95% purity) and room air were investigated.

It was observed that the majority of parameter changes did not affect the electron density significantly. This is believed to be due to the simple fact that the parameters were not varied strongly enough to see a significant change in density. However, stronger changes in density were observed in changes to the electrode and from mixtures of gases.

5.4.1 Effect of Operating Conditions on Plasma Electron Density

An extensive study to access the sensitivity of electron density to changes in discharge operating conditions was completed. Argon and helium discharges were studied. As electrons are the primary drivers of chemistry, identifying external operating parameters that have an effect on the density is important in designing a chemically focused discharge. In these studies, the following operating conditions are considered baseline and apply:

1. H_α was measured with a 10 micron slit and H_β with a 15 micron slit
2. The discharge was operated at a frequency of 5 kHz
3. The discharge voltage was approximately 2 $kV_{pk\text{-}pk}$
4. The discharge current was approximately 200 $mA_{pk\text{-}pk}$
5. The discharge electrode was tungsten rod.

5.4.1.1 Sensitivity to Discharge Voltage & Gas Flow

The effect of different discharge voltages on electron density was assessed, and was found to have little effect on density for the conditions investigated. Increasing the voltage amplitude increases the discharge current of the plasma, and was found to minimally increase density for both argon and helium plasmas (Figure 5.4). The sensitivity to frequency (1kHz versus 5 kHz)

[38] It is presumed that the jet can be operated using any gas, as it can be successfully operated with helium (the largest first ionization potential); however, only argon, helium, nitrogen and room air were actually investigated.

on density was also found to have little variation (Figure 5.5). For both data sets, the adjustments in parameters were most likely too small to have significant impact on the discharge, as the uncertainty in these measurements is on the order of $1x10^{20}$ m^{-3}.

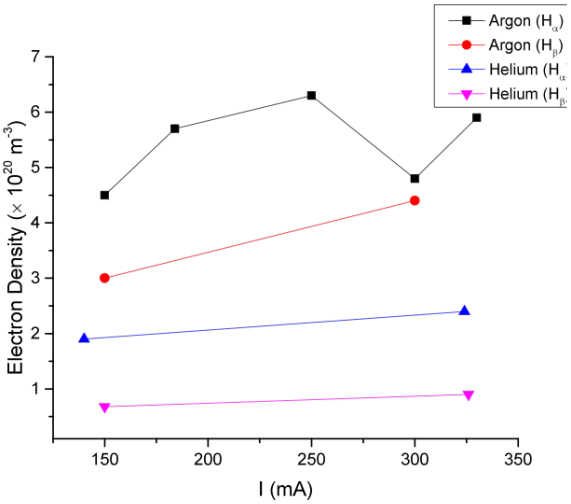

Figure 5.4: Changing plasma current and resulting electron density. Flow rates: Ar, 1.9 SLPM; He, 4.4 SLPM.

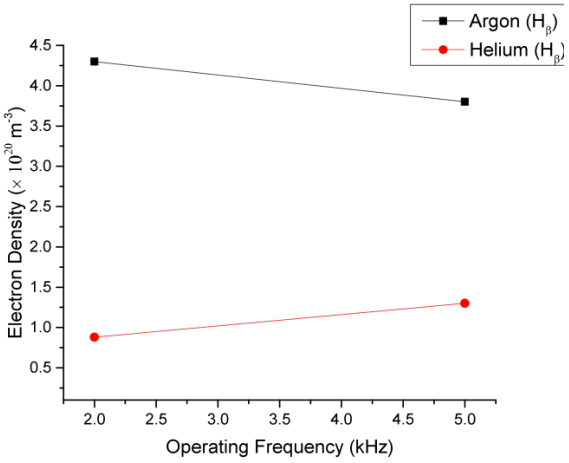

Figure 5.5: Effect of operating frequency on electron density.

The gas flow rate was varied as the amplitude of the plasma current was held at 200 mA for all discharges. The argon plasma was operated at flow rates between approximately 1.5 SLPM and 2.8 SLPM, and the helium plasma was operated between 3.2 SLPM and 6.9 SLPM. The plasma will not ignite for helium flows of 1.95 SLPM and below. The results may be seen in Figure 5.6.

The plateau in both the argon plasma electron density and helium plasma electron density from the H_β line is presumed to most likely be the result of some error in measurement due to the bubbling of the system that limits the sensitivity of the measurement (see discussion in Chapter 3). In addition, it is believed the system requires greater gas flows to see a greater change in density.

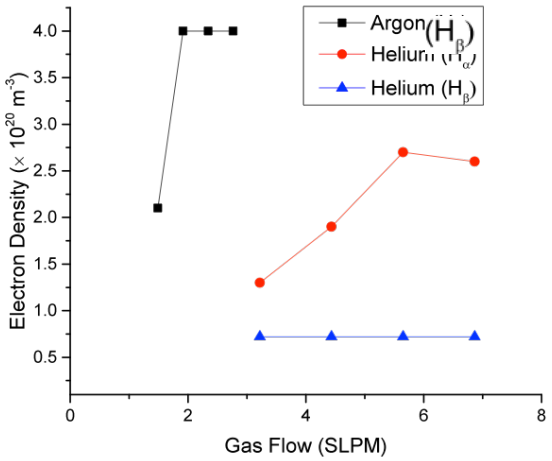

Figure 5.6: Electron density flow rate sensitivities.

5.4.1.2 Sensitivity to Electrode Material Type

For both the argon and helium plasmas, changing the electrode material from tungsten rod to copper high voltage wire reduced the electron density as shown in Figure 5.7. The electron density was measured both via the H_α and the H_β line. The argon flow was approximately 1.9 SLPM and helium flow approximately 4.4 SLPM.

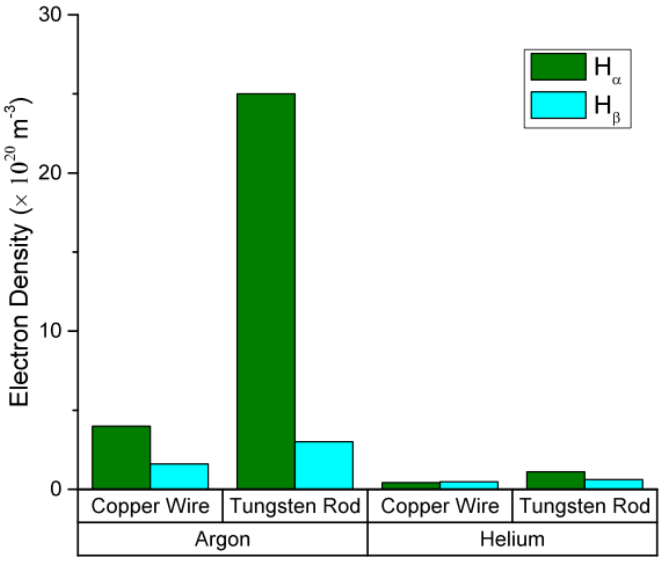

Figure 5.7: Effect of electrode material on electron density.

As the results from this section are time averaged, one possible explanation for the tungsten electrode to produce a denser plasma may be related to cathode phenomena, such as thermionic emission, which may boost the density. In addition, the secondary electron emission coefficient for tungsten is higher than for copper [**366**], which may play a role in the increase as well.

5.4.1.3 Changing Discharge Electrode Position

Here, the position of the discharge electrode within the quartz discharge tube was varied and the effect on electron density was assessed. In Figure 5.8, position refers to the distance the electrode was located from the exit of the quartz discharge tube. Again, the argon flow was approximately 1.9 SLPM and helium flow approximately 4.4 SLPM.

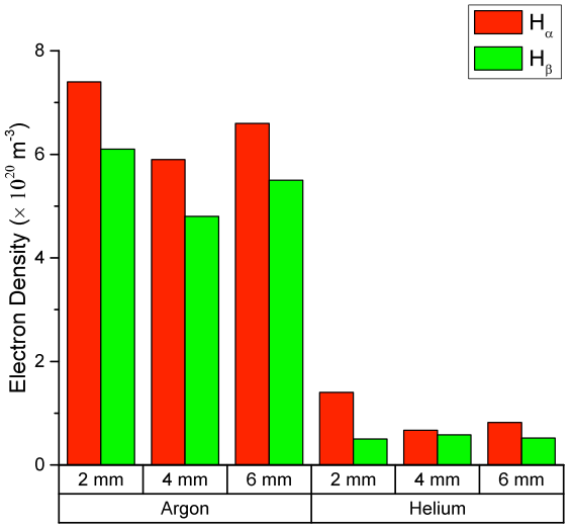

Figure 5.8: Effect of discharge electrode position on electron density.

For both plasmas, it is unclear if the position of the electrode relative to the exit of the discharge tube affects the electron density. While further work will be necessary, results suggest for both gases position 1 (2 mm from discharge tube entrance) has the greatest density, followed by position 3 (6 mm) and then position 2 (4 mm). This may be due to an increase in gas temperature: as position 3 corresponds with the longest path length, the longer transit may translate to a higher gas temperature. This higher temperature could increase electron production depending on the reaction mechanisms that become available to a higher temperature. The gas temperature was not measured during this study so a stronger assessment cannot be made. Further study with greater electrode positions is recommended.

5.4.2 Gas Mixtures

Mixtures of argon, helium and air were studied. Mixes of gases of have various benefits, allowing the qualities of one gas (e.g., ions in a helium plasmas deliver more energy than heavier ions) while incorporating another to compensate for a shortcoming of the first. Mixes give the ability to optimize source efficiencies (e.g., argon has a lower ionization potential than helium;

mixing argon with helium would reduce the input energy demands of a pure helium system), crucial to an ideal system design.

These studies used the H_α line only to deduce electron density due to poor collection of the H_β line. The slit opening of the monochrometer was 5 microns.

5.4.2.1 Helium Plasma with Increasing Argon

A helium plasma was ignited and argon was added at various flow rates (see Figure 5.9). The flow rate of helium was 5.33 SLPM and the flow rates of argon were 0 SLPM, 1.21 SLPM, and 2.41 SLPM.

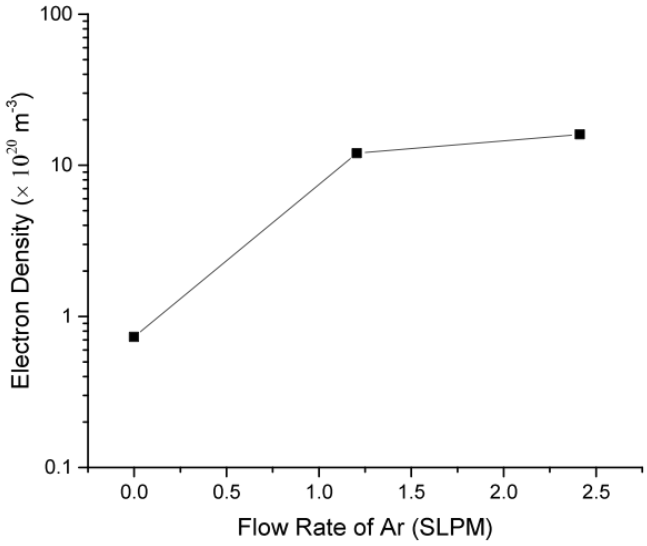

Figure 5.9: Effect on electron density of adding argon to a helium plasma.

The effect of adding argon to a helium discharge has a substantial effect on electron density from a pure helium plasma, though the effect appears to plateau as the ratio of molar quantities of helium and argon approach unity. This result is consistent with other works involving He-Ar discharges (e.g., [**367**]).

5.4.2.2 Argon with Air and Helium with Air Plasmas

The effect of adding air to argon or helium was also considered, and the results are shown in Figure 5.10. Adding air to a noble gas would increase the reactivity of discharge due to the resulting RONS (reactive oxygen and nitrogen species). The flow rate of argon was 3.83 SLPM and the flow rate of helium was 9.73 SLPM. The two flow rates of air considered were 0 SLPM and 0.944 SLPM.

Figure 5.10: Effect on electron density of adding air to an argon plasma (left) and helium plasma (right).

The electron density of the argon and the argon + air cases did not vary measurably between each other. However, the effect of adding air to the helium jet increased the electron density substantially. This is most likely due to the lower ionization potential of nitrogen than helium. It was observed in both argon and helium discharges that the addition of air increased the discharge voltage of the plasma. This may be due to increased Penning ionization between argon or helium and the introduced nitrogen [**368**].

For both argon + air and helium + air plasmas, quenching was observed for many of the non-nitrogen species. As an example, Figure 5.11 illustrates the reduction in oxygen and tungsten lines upon the addition of air in the system. The introduction of air to the system causes the discharge to become more contracted, resulting in less erosion. However, nitrogen species are preferentially populated and tend to quench energetically favorable levels of neighbors, so many of the species easily observed in either the argon or the helium discharges will be far less intense after the addition of air, as seen in Figure 5.11.

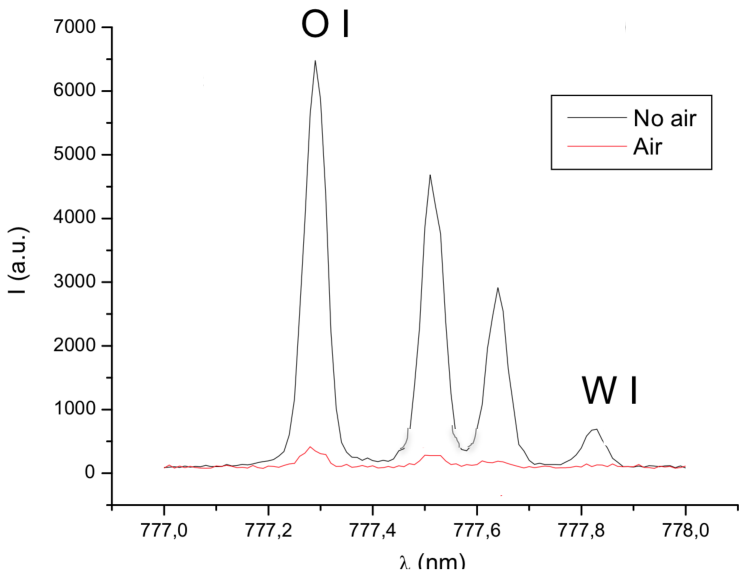

Figure 5.11: Example of the presence of nitrogen species depopulating other lines. Shown is the oxygen triplet near 777 nm and W I at 777.781 nm.

5.4.3 Summary

At similar flows and voltages of the gases considered, the electron density was highest for the argon plasmas. The effect of adding air to an argon plasma was not seen to affect the electron density appreciably. However this was not the case with the helium plasma, as adding only as much as 0.944 SLPM of air to a helium plasma did noticeably increase the electron density.

In general, the presence of air quenched most states of interest, most notably the hydrogen states as inferred from the observed emission intensity decrease, which effects the electron density measurement. Interestingly, the argon plasma with nitrogen was observed to increase the Na I population. As sodium is believed to originate from the discharge quartz tube, it is assumed that the presence of nitrogen couples to the sodium states. From an engineering prospective, the increase of sodium is an indicator of degradation of the discharge tube, and should be avoided.

Although helium plasmas tend to exhibit lower electron densities than argon plasmas, helium plasmas were observed to produce greater quantities of hydrogen species. This may be due to the helium plasma's ability to break more water bonds. However, as the plasma electrons are the primary drivers of chemistry, further study is recommended if the goal is feasible water purification.

5.5 Asymmetric Discharge[39]

5.5.1 Initial Observations

Unaided visual observations of the discharge suggest an even, non-changing plasma jet (as in Figure 5.1). However, the use of time-resolved measurements reveals the dynamic behavior of these discharges. A photodiode detector (1 ns rise time, 350 MHz operation frequency) was used to time-resolve the light intensity output of the discharge. For the range of frequencies used in normal operation/decomposition experiments (1 kHz to 5 kHz), it was discovered that the air discharge was most intense during the negative-going half of the cycle (see Figure 5.12 and Figure 5.13). In some operating conditions (appears to be power dependent, occurring with higher power depositions), the plasma appears to be two different discharges (i.e., streamer and arc-like).

As seen in Figure 5.12, the discharge undergoes two physically different discharge modes – the peak of the positive cycle, seen in Figure 5.12, frames b and c, resembles streamer discharge. In comparison, Figure 5.12, frame e, the peak output of the negative cycle, is not only much brighter (this is expected from the photodiode results) but also appears to be an arc-like discharge to the grounding coil. In addition, the current trace of the discharge (seen in Figure 5.13) shows the negative portion of the discharge cycle to be more intense.

[39] Work presented here has been presented at least partially in some form in the following [**433**,**97**,**434**]:

1. S N Gucker, M C Garcia, and J E Foster, "Optical Emission Spectroscopy of an Underwater DBD Plasma Jet," in *31st International Conference on Phenomena in Ionized Gases*, Granada, Spain, 2013, pp. ICPIG PS3-039.

2. Sarah Gucker, Maria García, Benjamin Yee, and John Foster, "Time Resolved Spectroscopy: Dynamic Study of a Dielectric Barrier Discharge Plasma," in *65th Annual Gaseous Electronics Conference*, Austin, TX, 2012.

3. S N Gucker, M C Garcia, and J E Foster, "Time resolved spectroscopy of an underwater dielectric barrier discharge plasma jet," in *39th IEEE International Conference on Plasma Science*, Edinburgh, Scotland, 2012.

5.5.2 Spectroscopic Investigation

Spectroscopic techniques are used to verify the bimodal findings, as the difference in discharge modes should result in a difference in species production. As an example, the

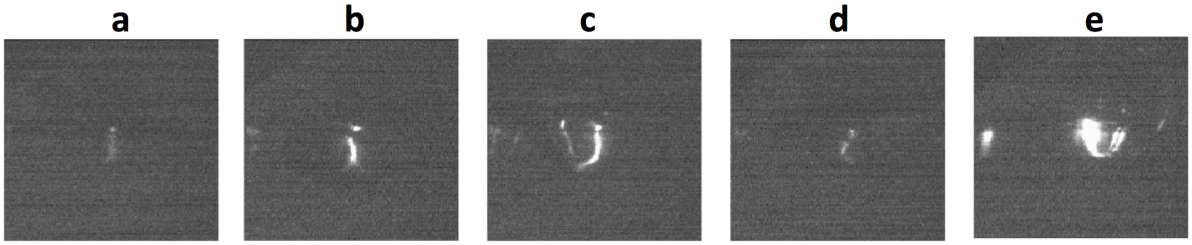

Figure 5.12: (a) t = 0, the voltage zero crossing; (b) t = 200 µsec, near peak of positive voltage and current; (c) t = 400 µsec, in the positive peak; (d) t = 500 µsec, peak negative voltage, minimum of emission; (e) t = 800 µsec, middle of negative voltage and peak current, peak of emission.

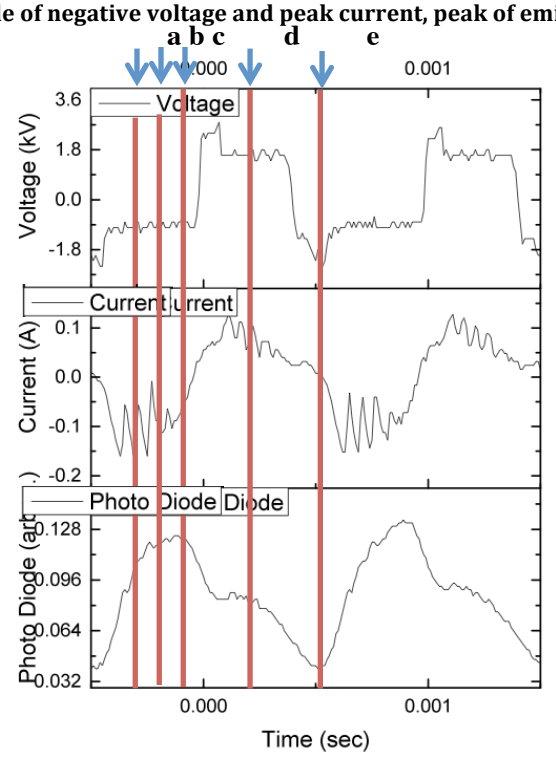

Figure 5.13: Approximate temporal locations of the images in Figure 5.12.

increased emission of electrode material (tungsten and molybdenum) during the negative cycle would suggest arc-like behavior (see Figure 5.24).

While the motion of the unstable bubble perturbs optical emission runs, thereby producing temporal distorted photographic images, the asymmetric quality of the underwater DBD plasma is seen regardless of gas type used. In the studies discussed in this work, the *total* light production was observed to occur during the negative portion of the discharge cycle for all investigated gases. However, the emission of *individual* plasma species has been observed to

depend on the source gas used. Unlike the photographs, the bubbling action is believed to not affect the spectroscopic results as the speed of the ICCD (shutter speed and number of exposures, which extends the length of time for a collection) is substantially faster than the time scale of the fluid motion (time scales of ~10 ms for fluid motion versus ~ns for gate timing).

Rotational gas temperature was determined via peak fitting of the OH (A-X) and N_2^+ (B-X) bands. The spectra were simulated using LIFBASE software developed by Luque and Crosley [**323**]. These temperatures have a typical range of 1800 – 2500 K for the plasmas investigated, though higher temperatures up to 3200 K are possible.

5.5.2.1 Electron Density – Polarity Effect

The effect of gas type and voltage polarity on electron density was determined. Example data may be found in Figure 5.14. A summary of the average results may be found in Table 5.2.

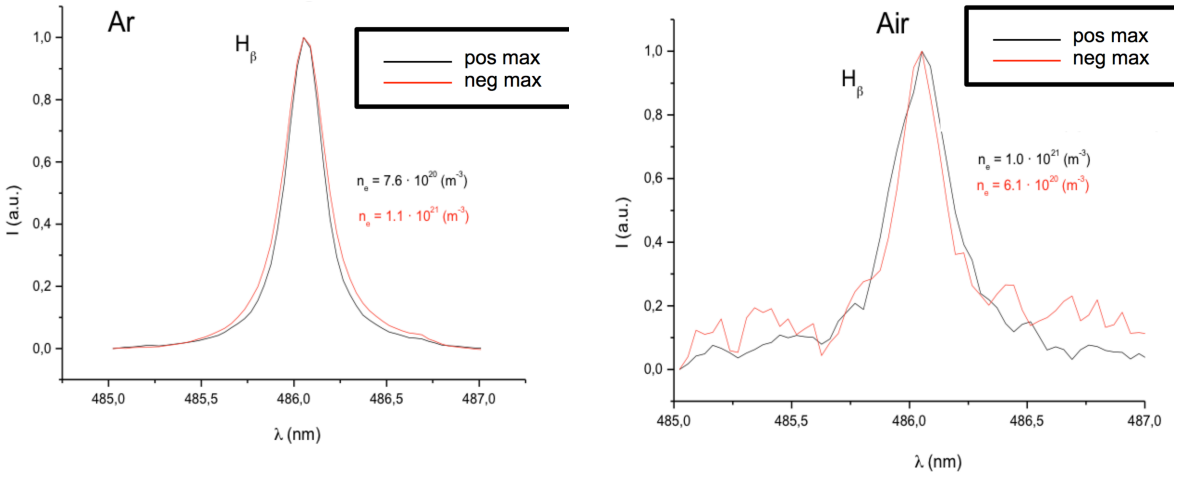

Figure 5.14: Variance of electron density on gas type and voltage polarity. Left, argon discharge. Right, air discharge. Electron density calculated via H_β.

Table 5.2: Electron density as a function of gas and voltage polarity.

	Electron Density ($\times 10^{20}$ m^{-3})			
	via H_α		via H_β	
	pos. peak	*neg. peak*	*pos. peak*	*neg. peak*
Air	44.0	16.0	10.0	6.1
Argon	23.0	35.0	7.6	11.0
Helium	1.1	5.4	0.6	3.6
Steam [**369**]	70.0	20.0	23.0	3.0

For the two noble gases, electron density is higher in the negative portion of the voltage cycle. For air and steam, electron density is higher (sometimes considerably more so) in the positive

peak. These results may be a reflection of the nature of positive versus negative streamers and the electronegative nature of the air and steam discharges.

5.5.2.2 Controlling Species Production

An overview of the various results may be seen in Figure 5.15 through Figure 5.22. A typical discharge voltage cycle trace may be seen in Figure 5.17 for reference.

5.5.2.2.1 Gas Temperature

Gas temperature (as determined via OH(A-X) band fitting with LIFBASE) was observed to be greater in the positive portion of the discharge voltage cycle for helium than for air or argon (Figure 5.15). For air plasmas, the 391 nm N_2^+ band also correlated to a greater gas temperature (Figure 5.16). Examples of temperature simulations to determine gas temperature via LIFBASE may be seen in Figure 5.18 and Figure 5.19 for a helium plasma (positive and negative peaks of the cycle, respectively).

5.5.2.2.2 Plasma Species: Oxygen Behavior

In addition to OH, another example of plasma species over the cycle is the O I 777 nm triplet. The oxygen species were observed to be more similar over the discharge cycle for the gases investigated (see Figure 5.19).

5.5.2.2.3 Electrode and Discharge Tube Material

In Figure 5.20 and Figure 5.21, electrode material is observed to also have a polarity dependence. Similarly, Figure 5.22 is the emission of sodium over the discharge cycle, believed to originate from the discharge tube. Avoiding damage to the system is an attractive possibility that should be investigated, and is just one example of how controlling species production would be highly beneficial to the development of a device.

5.5.3 Closing

As the species production has a voltage polarity and gas dependence, it should follow that the induced chemical reactivity within the bulk liquid would also manifest a polarity and gas

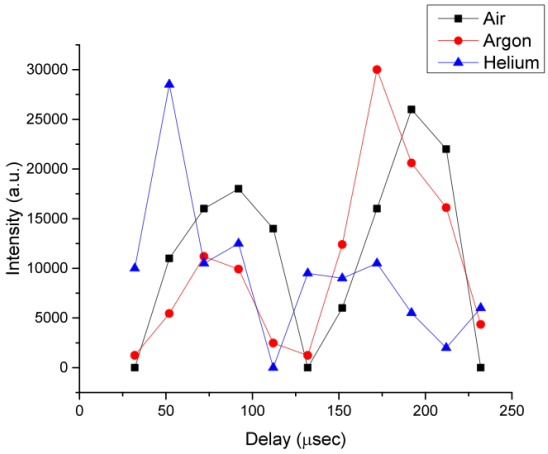

Figure 5.15: Intensity of the OH(A-X) (0,0) 308.9 nm peak over a voltage cycle for air, argon and helium.

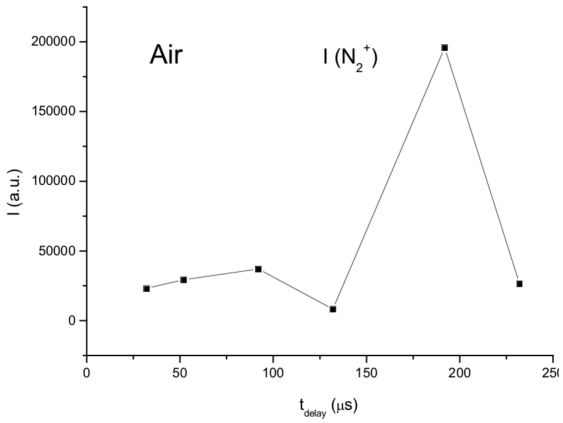

Figure 5.16: N_2^+ (B-X), 391 nm band. Neg. peak corresponds to ~2500 K. X).

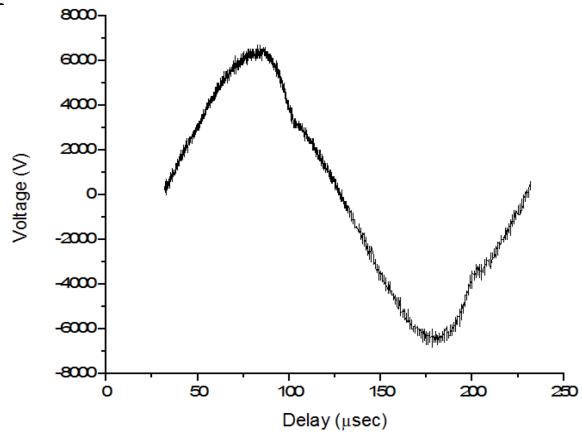

Figure 5.17: Typical discharge voltage cycle.

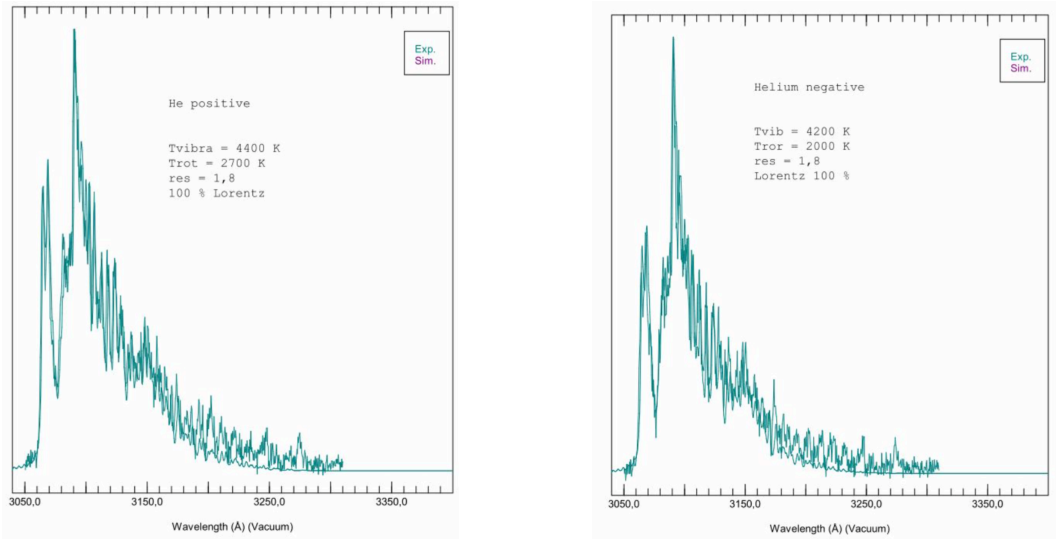

Figure 5.18: Simulated OH(A-X) band in LIFBASE to calculate rotational temperature. Helium plasma: left, positive intensity; right, negative intensity.

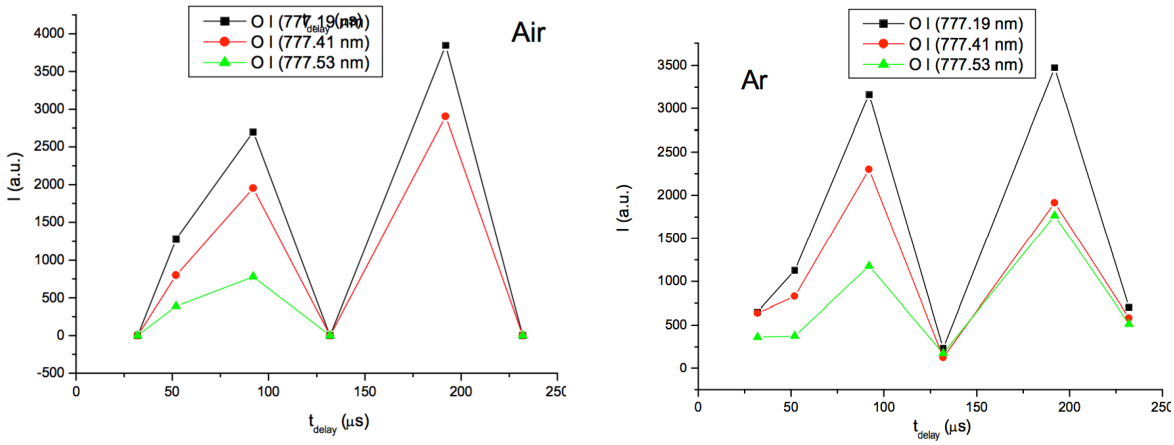

Figure 5.19: Intensity of the O I triplet over a discharge cycle for air (left) and argon (right) plasmas.

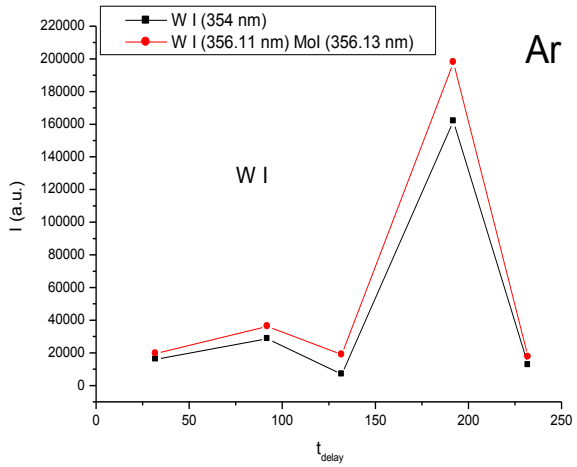

Figure 5.20: Electrode species (W I, high voltage electrode; Mo I, ground), argon plasma.

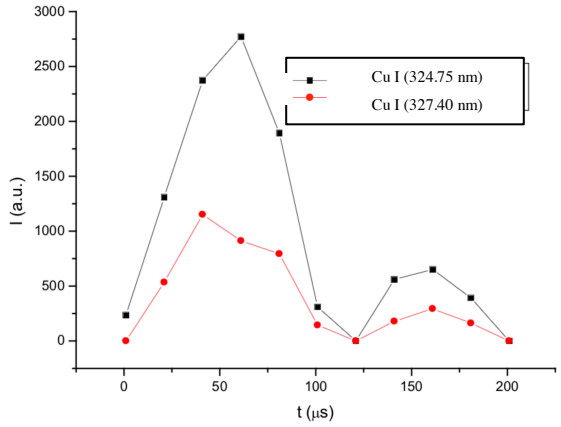

Figure 5.21: Electrode species (Cu I, both electrodes), helium plasma.

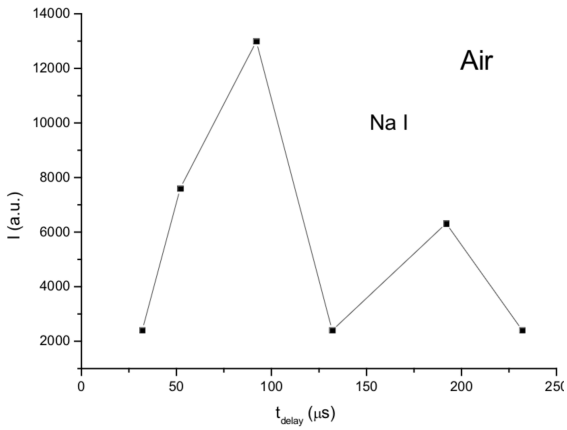

Figure 5.22: Na I from quartz discharge tube, air plasma.

dependence. Understanding the various dependences is a fundamental step toward realizable water purification (or associated fields, such as plasma medicine). Selectively adjusting the

physical characteristics of the system (establishing "knobs") to orchestrate the desired chemical mechanisms are key.

5.6 Contaminant Decomposition

To study the efficacy of plasma as a purifying agent, several decomposition studies were conducted. The contaminants used in these experiments were methylene blue dye, assorted halogenated compounds, and algae-laden water from a salt pond. These experiments were all performed with the DBD plasma jet. All experiments were performed with room air as the feed gas for the plasma discharge. Unless noted otherwise, all experiments were powered via 5 kHz sinusoidal voltage, which varied in amplitude approximately from $2kV_{pk\text{-}pk}$ to $14\ kV_{pk\text{-}pk}$. Current varied roughly from $200\ mA_{pk\text{-}pk}$ to $360\ mA_{pk\text{-}pk}$. Typical power consumption of the plasma ranged roughly between 50W and 150 W.

5.6.1 Methylene Blue

The bulk of the studies were performed with a common dye, methylene blue ($C_{16}H_{18}N_3SCl$, see Figure 5.23). Methylene blue (abbreviated to MB) has a multitude of uses, including application as a biological stain, chemical and biological indicator, multiple pharmaceutical applications (common antimalarial drug) and as a textile dye.

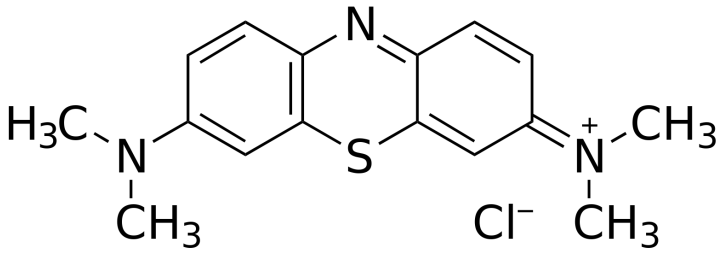

Figure 5.23: Structure of methylene blue.

As mentioned previously, textile runoff is the largest producer of polluted water by volume globally [**269**]. Every year approximately 1×10^6 kg of dyestuffs is ejected into the environment [**5**]. These massive volumes of polluted water pose a serious environmental health issue. One example may be seen in the surrounding plant life, as large concentrations of dyes reduce the photosynthesizing ability of the plant, which disturbs the whole food web. For animal life, many dyes, including MB, are converted into carcinogenic aromatic compounds when ingested by microbes and decomposed anaerobically [**370**].

5.6.1.1 Methylene Blue Decomposition Studies

MB is a common contaminant used by plasma scientists to study the efficacy of plasma waste decomposition [**371**,**372**,**274**,**373**,**50**]. The results of a decomposition trial carried out during the course of this dissertation research may be seen in Figure 5.24. Similarly to plasma discharges operated in liquid water (see Figure 5.2), processing a MB solution with an air plasma will produce similar pH and conductivity curves (see Figure 5.26). In addition to the acids produced by the plasma-air-water system (e.g., especially nitrous and nitric acid [**73**]), the daughter products of the MB molecule as it is broken down can play an important role.

5.6.1.2 Experimental Methods

To assess the time rate of change of the decomposition process of a contaminant, the liquid was metered for pH and conductivity changes at various time intervals. In addition, liquid samples were taken to be analyzed via spectrophotometer and/or mass spectrometry. Discharge voltage and current were monitored throughout the process. MB was decomposed via two different modes, the plasma jet mode and the microdischarge mode. The concentration of dye was approximately 50 mg/L, or roughly 0.15 mM. Volumes of 100 mL were treated in each run. The discharge voltage was 2 kHz, ~4 kV_{pk-pk}. Both modes were operated with room air as the feed gas at 1.65 SLPM flow rate. Please refer to the waveforms in Chapter 3 (Figure 3.9 through Figure 3.14) for typical waveforms of these two modes.

5.6.1.2.1 Molecular Assessment

While the degradation of a dye can be achieved with atmospheric plasma discharges, it is not always clear as to the nature of the decomposition products. Thorough assessment of the plasma-treated by products is essential. If the technology is to progress beyond the laboratory bench and into the realm of real world application, it is paramount that the decomposition products be quantified and toxicity accessed. An example of neglect of such consideration in the ozonation of MTBE (methyl-*t*-butyl-ether, a gasoline additive and predominant groundwater pollutant): incomplete oxidation of MTBE during ozonation creates daughter products that are as or *more* toxic than MTBE itself [**374**].

Figure 5.24: Samples of a methylene blue plasma jet decomposition trial, from t = 0 (leftmost) to t = 5.5 minutes (rightmost). Samples taken every 30 seconds, two rightmost samples taken 60 seconds apart [375]. ~4 kV_{pk-pk}, 2 kHz, 1.65 SLPM flow rate of room air.

Figure 5.25: MB treated by microdischarge (~5 W). Samples range from t = 0 to t = 46 minutes of treatment time.

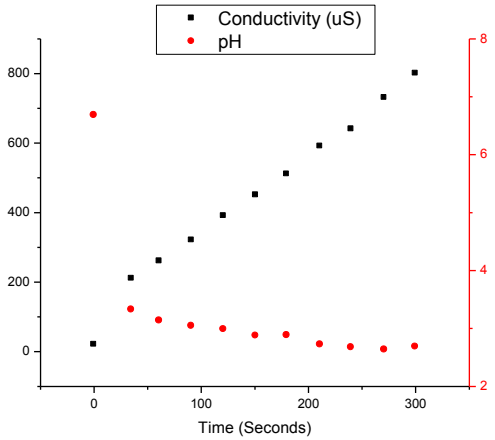

Figure 5.26: Change in plasma treated MB solution pH and conductivity with treatment time [375]. Data are from samples shown in Figure 5.24 [375].

5.6.1.3 Formation of Precipitate

Solutions were observed after ~2-6 hours post-processing. A precipitate was observed e at the bottom of the liquid. The relative amount of precipitate appeared to scale with the processing time. This is seen in Figure 5.24, where the precipitate at the base of each sample vial increases with processing time. (In Figure 5.25, the precipitate is only visible in the middle sample.)

Removal in a real system can be provided via filter. Analysis of the precipitate is left to future work.

Figure 5.27: Precipitate of processed methylene blue in solution, various images.

5.6.1.4 HPLC Results

To identify the degradation of the dye on a molecular level, HPLC mass spectrometry is used. However, molecular assessment of plasma-treated solutions can be challenging due to the physical and chemical plasma processing the solution undergoes during plasma treatment (this is in comparison with traditional wet chemistry). HPLC requires the analyst to know attributes about the sample – plasma discharges have the ability to chemically but also physically break bonds, creating a mixture of disjointed molecules. This is immediately apparent in the HPLC results (Figure 5.31). The peaks at lower m/z values (in comparison to the MB m/z peak at 284, e.g., 123 m/z peak in Figure 5.31.d) are most likely a benzene ring with a highly branched substitute. The peaks at higher m/z are most likely due to the formation of the particulate that precipitates out of solution with plasma processing. Future work requires the analysis of this precipitate, as it should unveil a host of chemistry pertinent to further developing this work.

It should be noted that only positively charged species are detected by this method (ESI-MS); radicals, which are electrically neutral, will not be detected. The results will vary depending on gas type used, which indicate different physical chemical mechanisms (see Chapter 6 for a comparison between an air and steam plasma jet processing MB). The difference in daughter

product peaks is possibly another knob for controlling the plasma properties to develop an optimal decomposition device.

5.6.1.4.1 Methylene blue processed by plasma jet

The plasma jet was run for 5.5 minutes at approximately 75 W. The visual results may be seen in Figure 5.24 and the molecular analysis via HPLC may be seen in Figure 5.30. Although the color appears to the eye to be almost all gone from the solution, upon inspection of the mass spectroscopy results it is clearly apparent that the MB molecule (M = 284 m/z) has just started to be broken down. Upon examination of the results, three peaks of various degradation stages may be identified: 1, the loss of a methyl group from the main methylene blue cation (M = 269 m/z, Figure 5.28); 2, the probable formation of a sulfoxide (M = 303 m/z, Figure 5.29); and 3, the possible loss of a second methyl group (M = 254 m/z, Figure 5.28). The formation of the sulfoxide arises from the OH attacking the free doublet of the sulfur atom in the center of the methylene blue ion. Due to the conservation of double bond conjugation, the central ring opens (as seen in Figure 5.29); it has been hypothesized by various authors that the breaking of the central benzene ring is key to rapid decomposition of the dye [**376**].

Similar results have been seen in oxidation studies of methylene blue as well as studies on alcohol dehydrogenation and pesticide degradation. [**377**,**376**]. The results suggest that OH is the primary driver of decomposition, at least for the primary breakdown.

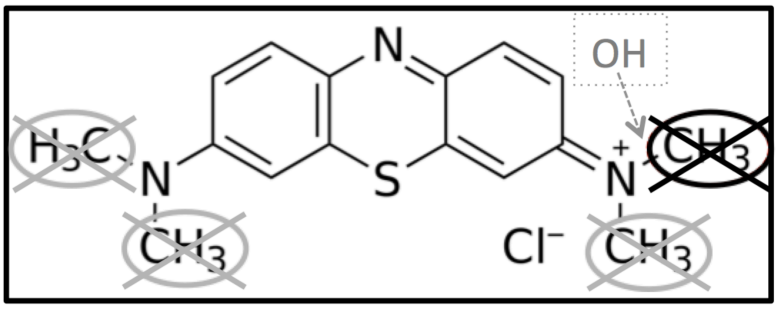

Figure 5.28: Loss of the primary (black) and secondary (gray) methyl groups of the main methylene blue cation (peaks 1 and 3 in Figure 5.30). Note that only one of the grayed methyl groups would be lost.

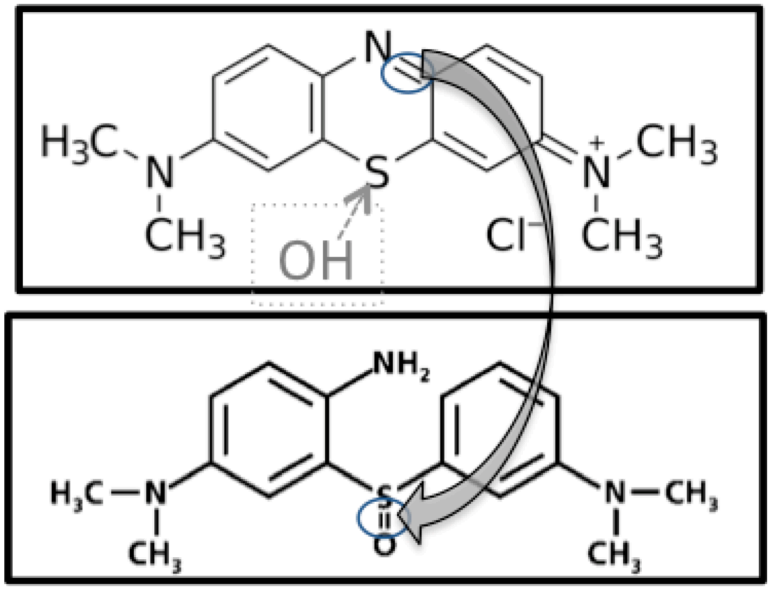

Figure 5.29: Formation of sulfoxide from the main methylene blue cation (peak 2 in Figure 5.30). Conservation of double bond conjugation results in the central ring opening up.

5.6.1.4.2 Methylene blue processed via microdischarge mode

The plasma was operated in the microdischarge mode for 56 minutes at approximately 5 W, as seen in Figure 5.25 (molecular analysis via HPLC is shown in Figure 5.31). Again, it is well past the point the color appears to the human eye to be removed from the liquid that the MB peak is seriously degraded and daughter products emerge. Only until Figure 5.31.d do discernable peaks begin to arise, and even then, only two peaks are readily identifiable. The first peak is the same as the jet results, the loss of a methyl group (CH_3) appears at 269 m/z. The second peak at 123 m/z is possibly nitrobenzene ($C_6H_5NO_2$), which would have originated from a branched substituted benzene from the parent MB molecule. Additional chemical diagnostics are necessary to confirm the presence of this compound; if it is possible that microdischarges in MB can breakdown and reform pieces of the parent molecule to form nitrobenzene, care is essential as nitrobenzene is highly toxic (limit for workers is 5 mg/m^3/day).

5.6.1.4.3 Comparison

Figure 5.32 summarizes the results of the two decomposition trials. The jet mode, though operated for a shorter amount of time and with a higher end concentration, had a faster

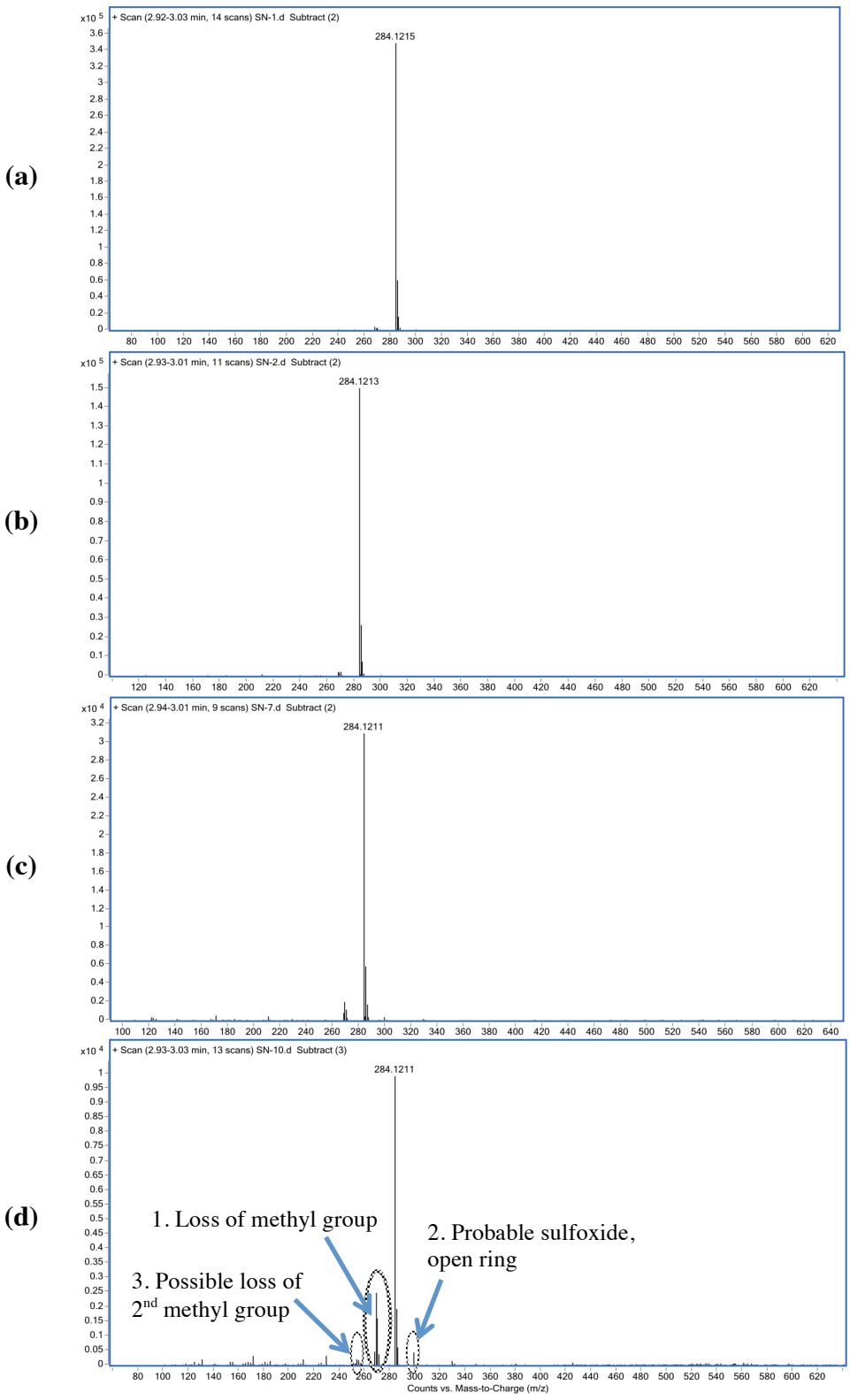

Figure 5.30: Counts vs Mass-to-Charge (m/z). (a) MB decomposed by air plasma jet at t = 0; untreated sample. (b) 30 s of plasma treatment. (c) 180 s. (d) 270 s.

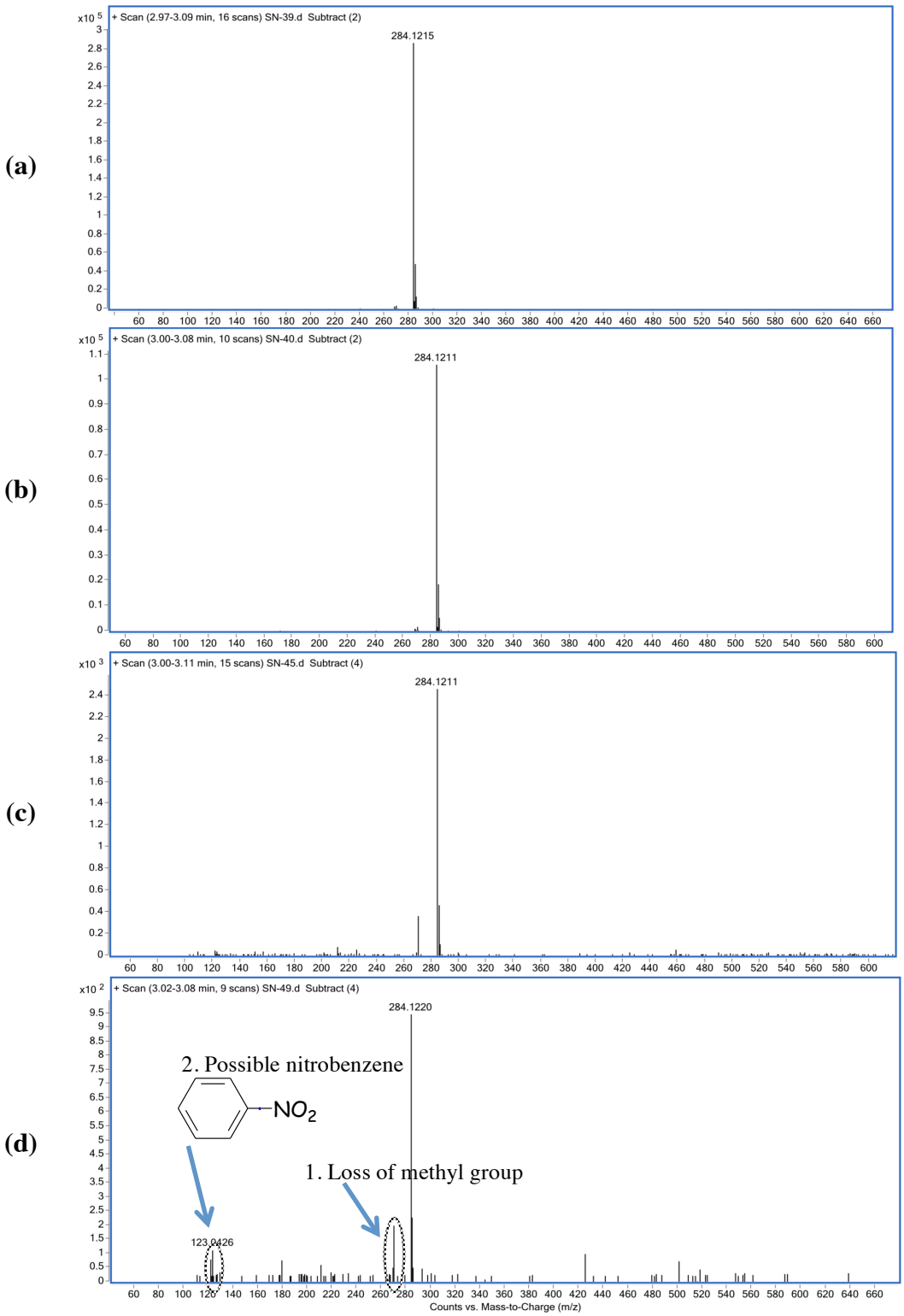

Figure 5.31: Counts vs Mass-to-Charge (m/z). (a) MB decomposed by air microdischarge. t = 0; untreated sample. (b) 5 minutes of plasma treatment. (c) 26 minutes. (d) 46 minutes.

decomposition with a time constant[40] of approximately 80 seconds from the relation. The microdischarge mode, on the other hand, had a time constant of approximately 480 seconds. Although the jet mode is slower, the computed G_{50} value (see (3.15)) for these processes is over 5 g kWh^{-1} for the jet mode versus a G_{50} value of roughly 10 g kWh^{-1} for the microdischarge mode. The microdischarge mode does have a few additional advantages, such as lower processing heat (the processed liquid stays at roughly room temperature throughout processing, even at long processing times of a few hours), which results in little to no loss of liquid via evaporation. The jet mode can result in significant evaporation if processing power is high. Similar comparisons were done in [**358**]. However, real-world application of plasma water treatment must be a timely process, and the slow processing of the microdischarge is not believed to a feasible method.

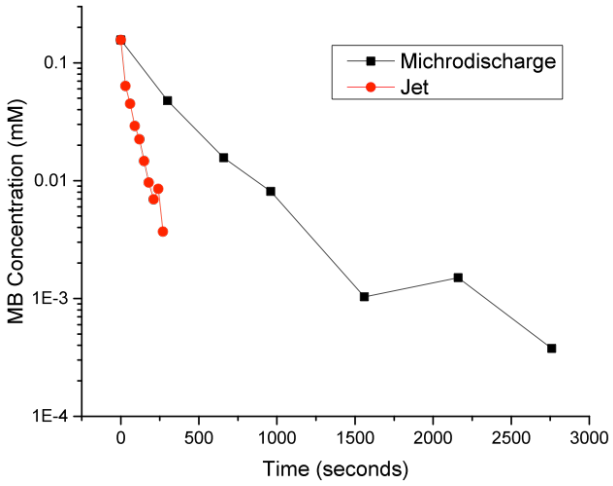

Figure 5.32: Decomposition of methylene blue by microdischarge and plasma jet.

5.6.1.5 Effect of Radical Scavenger [375][41]

To determine the effects of OH^- in the decomposition process, phosphate buffered saline (PBS) was added to the solution. PBS is a common buffer solution used primarily in the biological sciences to keep the pH of solutions constant. Due to the properties of PBS (i.e.,

[40] Here, the time constant is the amount of time for the solution to be reduced to 1/e times the initial concentration, from the relation $N(t) = N_0 e^{-t/\tau}$. This time constant only referring to the concentration of the MB molecule, not any of the daughter products.

[41] Subsection a partial synopsis of work published in IEEE Transactions on Plasma Science: S. M. Nowak and J. E. Foster, "Power studies of an underwater DBD plasma jet," in *2011 Abstracts IEEE International Conference on Plasma Science*, 2011 © IEEE 2011. doi: 10.1109/PLASMA.2011.5993390

neutralizing OH^-), processing a methylene blue solution with added PBS gives a qualitative measure of the impact of OH^-.

5.6.1.5.1 Experimental Method

The experiment repeated the jet decomposition experiment from the immediately preceding subsection but with the addition of PBS. The discharge voltage was 2 kHz, ~3.6 kV_{pk-pk} with an approximate power consumption of 75 W. Room air was the feed gas at 1.65 SLPM flow rate. The concentration of dye was 46 mg/L. PBS was pre-formulated in tablet form for easy mixing into test solution (Amresco, PBS tablets). The concentration of the PBS solution was 10 mM phosphate buffer, 137 mM sodium chloride, and 2.7 mM potassium chloride; all together, when combined with 100 mL deionized water creates a 1x (i.e., normal strength solution) PBS solution.

5.6.1.5.2 Results

Figure 5.33: Samples of MB with PBS treated by plasma jet. Leftmost vial, t = 0 (before plasma treatment); rightmost vial, t = 5 minutes. Samples taken roughly every 45 seconds.

It was found that the presence of PBS prohibited significant physical change in the solution for similar time scales (see Figure 5.33). Figure 5.34 shows the change in pH and conductivity of both the MB solution (samples shown in Figure 5.24) and of the MB + PBS solution (samples shown in Figure 5.33).